Robotica (2025), **43**, pp. 3976–4004
doi:10.1017/S0263574725102592

CAMBRIDGE UNIVERSITY PRESS

RESEARCH ARTICLE

Workspace analysis of a 6-degree-of-freedom hybrid robot with two parallel modules

Kirill Mukhin, Anton Antonov and Alexey Fomin

Mechanical Engineering Research Institute of the Russian Academy of Sciences, Moscow, Russia
Corresponding author: Alexey Fomin; Email: alexey-nvkz@mail.ru

Received: 15 March 2025; **Revised:** 4 August 2025; **Accepted:** 5 September 2025; **First published online:** 15 October 2025

Keywords: hybrid robot; relative manipulation; inverse kinematics; Delta-type mechanism; parallel mechanism with a circular rail; translation workspace; orientation workspace; link interference; discretization method; GJK algorithm; CAD simulation

Abstract

Workspace analysis is a crucial step in designing any robotic system and ensuring its safe operation. This article analyzes the workspace of a six degree-of-freedom (6-DOF) hybrid robot, which includes two separate modules with parallel architectures placed above each other. The upper module is a 4-DOF Delta-type parallel mechanism, and the lower module is a 2-DOF rotary mechanism with a circular rail. With this design, the hybrid robot represents a relative manipulation system, and workspace analysis is performed in the relative motion of the modules. This approach differs from other similar studies that combine the workspaces determined for each module independently, and we propose a method and derive results more suitable for practical use. To solve the workspace analysis problem, the paper develops a discretization-based approach, which considers all mechanical constraints. These constraints include joint constraints of each module and link interference between the modules. To analyze this interference, we apply the Gilbert–Johnson–Keerthi algorithm and represent the links as convex polytopes. Multiple numerical examples illustrate the developed techniques and show the translation and orientation workspaces of the robot for various relative configurations of its modules. Computer-aided-design simulations validate the proposed theoretical algorithms. The results demonstrate that the link interference between the modules, often ignored in other works, limits the workspace and should be considered for the proper workspace evaluation and design of similar hybrid robots.

1. Introduction

Hybrid robots represent mechanical systems composed of several modules, usually with serial or parallel architectures [1, 2]. Among them are relative manipulation systems, where these modules are placed individually on the base and operate together [3–5]. Such an arrangement improves the functional characteristics of the hybrid robot, which would be unreachable when using the modules separately or connecting them together. These characteristics include increased workspace dimensions and the reconfiguration ability depending on the application [6, 7]. Thanks to these benefits, hybrid robots with relative manipulation have become widespread in machining [8, 9], cooperative assembling [10, 11], additive technologies [12, 13], and medicine [14, 15].

Workspace analysis of robotic systems, including the hybrid robots mentioned above, is a fundamental problem of their design and performance evaluation [16–18]. The workspace defines the region where the robot can effectively perform manipulations, maintaining specified accuracy and stiffness or avoiding singularities [19]. Correct workspace determination enhances robot performance, prevents collisions between its links, and ensures safe operation. Scholars have proposed various approaches for workspace analysis, typically based on geometrical or numerical techniques [20].

Because of the widespread use of hybrid robots in modern applications, the problem of their workspace analysis and optimization has become the subject of many studies in recent years. At the same time, the workspace analysis methods differ according to the design features of the considered robot and

© The Author(s), 2025. Published by Cambridge University Press.

https://doi.org/10.1017/S0263574725102592 Published online by Cambridge University Press

the mechanisms of its modules. Thus, Tsai and Joshi [21] and Kucuk [22] analyzed workspaces using numerical methods with a random generation of points, which were expected to be inside the workspace. The inverse kinematics was solved for each point, and the condition number of the Jacobian matrix was computed to decide whether to include the point in the workspace. Chaudhury and Ghosal [23] and Zhang and Wei [24] followed a similar approach but applied a Monte–Carlo method, which resulted in a more accurate analysis of geometrical and kinematic constraints when solving the optimal design problem. In ref. [24], the authors used Monte–Carlo-based numerical optimization to determine the workspace of a manipulator with four degrees of freedom (4-DOF), considering its stiffness and kinematic parameters. Ye et al. [25] considered the symmetrical design of a 5-DOF robot to simplify their computations and experimentally verified the results of the workspace analysis on a physical prototype.

Smits et al. [26] studied a hybrid mechanism with a remote center of motion (RCM) applied to robotic eye surgery. During its workspace analysis, the authors examined the end-effector motion relative to the point positioned by another module of the mechanism. Another hybrid surgical robot with five DOFs and an RCM was considered by Pisla et al. [27], who determined the workspace of each module and then combined the results. The workspace constraints included the restrictions imposed by a medical tool. Rastegarpanah et al. [28] studied a 9-DOF foot rehabilitation robot with two modules and also combined the workspaces of the modules, including the stiffness criteria in the analysis.

Schreiber and Gosselin [29] considered planar mechanisms and followed another approach: the authors determined the workspaces of the individual kinematic chains and found their intersection. Xu et al. [30] applied a similar method to a 6-DOF hybrid robot for polishing freeform surfaces and showed it had no singularities in the prescribed task workspace. Singularities were also examined by Zhang et al. [31], who analyzed the workspace of a 5-DOF hybrid robot for high-speed machining of aerospace components. The authors applied a numerical approach and considered joint constraints.

Qin et al. [32] analyzed the workspace of a hybrid robot composed of two parallel cable-driven mechanisms. The authors considered geometrical and force constraints and determined the wrench-feasible collision-free workspace of the robot. Chawla et al. [33] solved a similar problem for another cable-driven robot, which was applied for 3D printing. The authors checked cable tension and interference between the robot end-effector and printed layers and determined the workspace that met both criteria.

The literature review shows that workspace analysis of hybrid robots with relative manipulation is a comprehensive problem. It is solved using analytical or numerical methods that consider geometric, kinematic, and force constraints, as well as singular configurations. Most existing studies, however, focus mainly on the independent workspace analysis of each module with the subsequent combination of the obtained results. This method can be suitable for computing translation workspaces [20], but it becomes more challenging to implement for determining other types of workspaces (orientation or reachable). At the same time, it is relevant to analyze the workspace in the relative motion of the modules, considering their cooperative work and possible interference of their links. This approach is more desirable in practice, where one module typically positions a tool and the other moves a processed object. The workspace analysis performed for the relative configurations of the tool and object ensures proper trajectory planning and safe operation with no collisions between the modules.

This paper shows how to solve this problem for a recently proposed 6-DOF hybrid robot composed of two modules with parallel architectures [34]. The major contribution of this work is the development of a concise approach that allows computing the workspace in the relative motion of two modules. It considers all mechanical constraints of each module, as well as possible collisions between its links.

The rest of this article has the following structure. Section 2 presents the design of the hybrid robot. Section 3 develops the algorithm of the workspace analysis. Section 4 illustrates the application of this algorithm with multiple examples, verified by computer-aided-design (CAD) simulations. Section 5 discusses some features of the proposed techniques and their potential improvements. Section 6 recaps the results and mentions directions for future studies.

https://doi.org/10.1017/S0263574725102592 Published online by Cambridge University Press

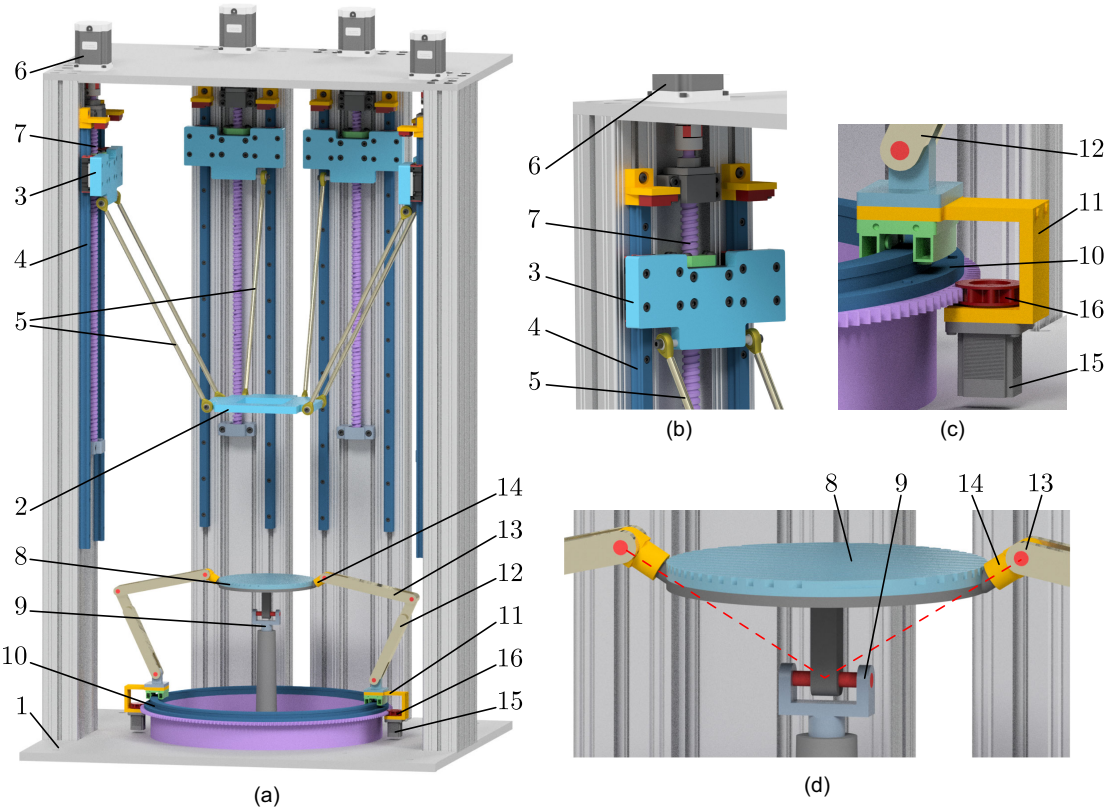


Fig. 1. *Computer model of the considered robot: (a) front view of the robot; (b) carriage of the upper module; (c) carriage of the lower module; (d) lower moving platform.*

2. Robot design

The considered hybrid robot consists of two separate modules placed above each other (Fig. 1). The upper module is a 4-DOF Delta-type parallel mechanism introduced in ref. [35] and studied in refs. [36–38]. It includes four kinematic chains (branches) connecting moving platform 2 with base 1: two central branches and two lateral branches. Each branch consists of carriage 3 that translates along linear guide 4. The central branches include rod 5 coupled with carriage 3 and platform 2 by spherical joints. The lateral branches include two similar rods that form a parallelogram sub-chain. Drives 6, placed on the base, actuate carriages 3 and transmit their motion via ball screws 7. This architecture provides moving platform 2 with a 4-DOF Schönflies motion type: three translational DOFs and one rotational DOF about the horizontal axis that points in front of the robot [37].

The lower module is a 2-DOF rotary parallel mechanism with a circular rail inspired by similar mechanisms proposed in refs. [39, 40] and spherical mechanisms that we analyzed in refs. [41–43]. The mechanism has three branches that connect moving platform 8 with base 1: one central branch and two lateral branches. The central branch includes yoke 9 rotating about the vertical axis, which coincides with the axis of circular rail 10. Yoke 9 attaches to platform 8 with a revolute joint, whose axis remains parallel to the horizontal plane. Each lateral branch includes carriage 11, lower bar 12, upper bar 13, and coupler 14. All these links are connected to each other by revolute joints, and their axes are parallel to each other and the horizontal plane. Coupler 14 attaches to platform 8 with a revolute joint, whose axis passes through the center of yoke 9. Drives 15, installed on carriages 11, actuate them via gear wheels 16. This architecture provides moving platform 8 with two rotational DOFs: unlimited rotation about the rail axis and tilt about the horizontal axis of the central branch.

https://doi.org/10.1017/S0263574725102592 Published online by Cambridge University Press

Thus, the hybrid robot has six DOFs in the relative motion of its moving platforms and can be used as a coordinate-measuring machine [44, 45]. The upper moving platform can position a measuring tool or a visual system, while the lower platform can orient a measured object. At the same time, such combination of the two modules improves the rotational capabilities of the robot, which are usually limited when using a single 6-DOF parallel mechanism [46]. Compared with a 6-DOF parallel mechanism, lower-DOF modules have simpler architectures with a smaller number of joint constraints that affect the reachable rotational angles of their output links. As a result, the relative rotational angles of these links increase. In the next section, we present an algorithm to analyze the workspace of the hybrid robot.

3. Workspace analysis

To analyze the robot workspace, we will follow a conventional discretization-based approach [47]. It relies on sampling the space of the end-effector configurations, solving the inverse kinematics, and checking the constraints. Unlike conventional serial or parallel robots, the considered robot includes two modules performing relative motions. Therefore, we will perform the workspace analysis in this relative motion. It means that we consider the workspace of the upper module relative to the lower one and do not consider their workspaces relative to the base. In this regard, the workspace analysis of the hybrid robot differs from the workspace analysis of serial or parallel robots.

The workspace shape and dimensions depend on mechanical and non-mechanical constraints. The former include joint constraints and link interference, and the latter are determined by singular configurations [48]. In this paper, we focus only on the mechanical constraints, while singularities, briefly discussed in Section 5, will be the subject of our upcoming studies. For the considered robot, these constraints are the following:

1. Joint constraints of the upper module, including displacement constraints for its carriages and rotational constraints for its spherical joints.
2. Joint constraints of the lower module, including collision avoidance for its carriages and rotational constraints for its revolute joints.
3. Link interference between the upper and lower modules.

The first two sets of constraints in the list above can be analyzed for each module independently. Therefore, the first step of the workspace analysis is to determine the posture of each moving platform relative to the base, as discussed in the next section.

3.1. Inverse kinematics of the relative motion

Before starting the analysis, we introduce three reference frames (Fig. 2). The first frame, $Oxyz$, is attached to the base. Its Oz axis coincides with the axis of the circular rail and points upward. The Ox axis points to the left branch of the upper module. The second frame, $O_1x_1y_1z_1$, is attached to the moving platform of the upper module. Its axes are parallel to the corresponding axes of the $Oxyz$ frame when the platform is horizontal. The third frame, $O_2x_2y_2z_2$, is attached to the moving platform of the lower module. Its O_2x_2 and O_2y_2 axes are parallel to the corresponding axes of the $Oxyz$ frame when the platform is not rotated and not tilted. The O_2z_2 axis passes through point F, where the axes of the central branch joints intersect. The origins of all the reference frames can be selected arbitrarily, ensuring that the conditions stated above are satisfied.

Now, we can specify the relative configuration of the modules using transformation matrix $\mathbf{T}$, which defines the configuration of frame $O_1x_1y_1z_1$ relative to $O_2x_2y_2z_2$:

$$\mathbf{T} = \begin{bmatrix} \mathbf{R} & \mathbf{p} \\ \mathbf{0}^{\mathrm{T}} & 1 \end{bmatrix}, \tag{1}$$

https://doi.org/10.1017/S0263574725102592 Published online by Cambridge University Press

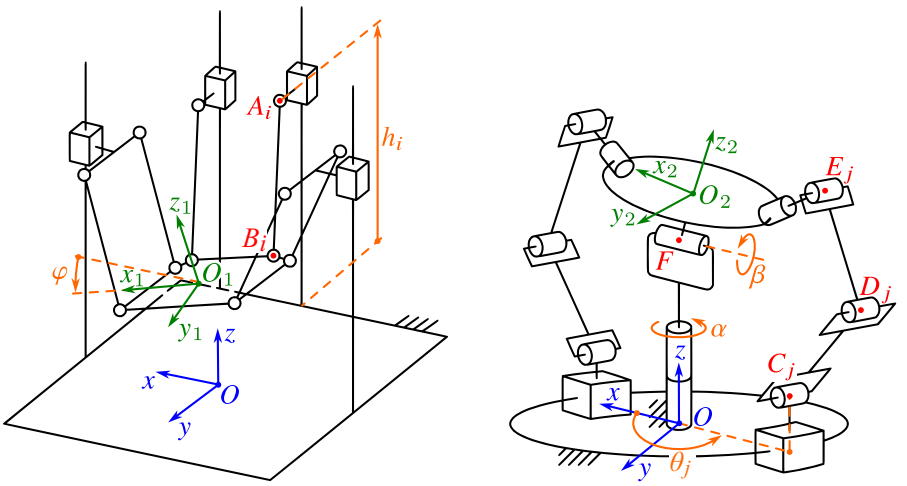


Fig. 2. *Kinematic schemes of the upper (a) and lower (b) modules and their reference frames.*

where $\mathbf{R}$ is a rotation matrix that defines the orientation of frame $O_1x_1y_1z_1$ relative to $O_2x_2y_2z_2$; $\mathbf{p}$ is a position vector of point O_1 relative to $O_2x_2y_2z_2$; $\mathbf{0}$ is a 3×1 vector of zeros.

The discretization approach of the workspace analysis implies sampling parameters $\mathbf{p}$ and $\mathbf{R}$. For example, if we determine the translation workspace, we set constant rotation matrix $\mathbf{R}$ and sample the components of vector $\mathbf{p}$. If we determine the orientation workspace, we set constant position vector $\mathbf{p}$ and sample the components of rotation matrix $\mathbf{R}$. In this case, it is convenient to parameterize the rotation matrix by three parameters (e.g., roll-pitch-yaw angles [49] or tilt-and-torsion angles [50]), simplifying the workspace representation.

Other types of workspaces can be determined by simultaneous discretization of the position and orientation parameters [47]. In any case, we assume that position vector $\mathbf{p}$ and rotation matrix $\mathbf{R}$ have some predefined values, for which we compute displacements in the joints and check the constraints. This computation involves solving the inverse kinematic problem for each module. Thus, we should first determine configurations of the modules relative to the base. We can specify these configurations by transformation matrices $\mathbf{T}_1$ and $\mathbf{T}_2$ that define the configuration of frames $O_1x_1y_1z_1$ and $O_2x_2y_2z_2$ relative to $Oxyz$, respectively (Fig. 2):

$$\mathbf{T}_1 = \begin{bmatrix} \mathbf{R}_y(\varphi) & \mathbf{p}_{O_1} \\ \mathbf{0}^{\mathrm{T}} & 1 \end{bmatrix}, \qquad \mathbf{T}_2 = \begin{bmatrix} \mathbf{I}_3 & l_{OF}\hat{\mathbf{z}} \\ \mathbf{0}^{\mathrm{T}} & 1 \end{bmatrix} \begin{bmatrix} \mathbf{R}_z(\alpha) & \mathbf{0} \\ \mathbf{0}^{\mathrm{T}} & 1 \end{bmatrix} \begin{bmatrix} \mathbf{R}_x(\beta) & \mathbf{0} \\ \mathbf{0}^{\mathrm{T}} & 1 \end{bmatrix} \begin{bmatrix} \mathbf{I}_3 & l_{FO_2}\hat{\mathbf{z}} \\ \mathbf{0}^{\mathrm{T}} & 1 \end{bmatrix}, \tag{2}$$

where φ is the tilt angle of the upper platform; α and β are the pan and tilt angles of the lower platform, respectively; $\mathbf{R}_x(*)$, $\mathbf{R}_y(*)$, and $\mathbf{R}_z(*)$ are the rotation matrices about the corresponding axes; $\mathbf{p}_{O_1}$ is a position vector of point O_1 in frame $Oxyz$; l_{OF} and l_{FO_2} are the distances between the corresponding points; $\mathbf{I}_3$ is a 3×3 identity matrix; $\hat{\mathbf{z}} = [0\,0\,1]^{\mathrm{T}}$.

Matrix $\mathbf{T}_1$ shows that the upper module configuration depends on four parameters: angle φ and three components of vector $\mathbf{p}_{O_1}$. The configuration of the lower module depends on angles α and β: the left and right transformation matrices in the expression of $\mathbf{T}_2$ are constant and correspond to the displacements along the Oz and O_2z_2 axes (Fig. 2). Thus, these are angles α, β, and φ and vector $\mathbf{p}_{O_1}$ that should be determined for specified matrix $\mathbf{T}$. The transformation matrices are related by the following equation:

$$\mathbf{T}_1 = \mathbf{T}_2\mathbf{T}. \tag{3}$$

https://doi.org/10.1017/S0263574725102592 Published online by Cambridge University Press

First, we consider the rotational part of Eq. (3). Substituting Eqs. (1) and (2) into this equation and rearranging the terms, we obtain:

$$\mathbf{R} = \mathbf{R}_x^{\mathrm{T}}(\beta)\mathbf{R}_z^{\mathrm{T}}(\alpha)\mathbf{R}_y(\varphi) \tag{4}$$

$$= \begin{bmatrix} \cos(\alpha)\cos(\varphi) & \sin(\alpha) & \cos(\alpha)\sin(\varphi) \\ -\sin(\alpha)\cos(\beta)\cos(\varphi) - \sin(\beta)\sin(\varphi) & \cos(\alpha)\cos(\beta) & -\sin(\alpha)\cos(\beta)\sin(\varphi) + \sin(\beta)\cos(\varphi) \\ \sin(\alpha)\sin(\beta)\cos(\varphi) - \cos(\beta)\sin(\varphi) & -\cos(\alpha)\sin(\beta) & \sin(\alpha)\sin(\beta)\sin(\varphi) + \cos(\beta)\cos(\varphi) \end{bmatrix}.$$

We can use Eq. (4) to find angles α, β, and φ for specified rotation matrix $\mathbf{R}$. Let r_{kl} be the (k, l)-th element of this matrix. Following the method from ref. [51, app. B], we compute two sets of solutions for these angles:

$$\begin{aligned} &\alpha = \operatorname{atan2}\left(r_{12}, \sqrt{r_{22}^2 + r_{32}^2}\right), && && \alpha = \operatorname{atan2}\left(r_{12}, -\sqrt{r_{22}^2 + r_{32}^2}\right), \\ &\beta = \operatorname{atan2}(-r_{32}, r_{22}), && \text{and} && \beta = \operatorname{atan2}(r_{32}, -r_{22}), \\ &\varphi = \operatorname{atan2}(r_{13}, r_{11}), && && \varphi = \operatorname{atan2}(-r_{13}, -r_{11}), \end{aligned} \tag{5}$$

where $\operatorname{atan2}(*, *)$ is the two-argument arctangent function [51, ch. 6].

We select the solution set for which angle $\beta \in [-90^\circ, 90^\circ]$, where the lower platform is not flipped. Note that Eq. (5) holds as long as $\alpha \neq \pm 90^\circ$, which corresponds to a singular configuration of the robot. In this configuration, the tilt axes of the upper and lower modules become parallel, and the robot loses one rotational DOF in the relative motion; each module, however, does not meet a singularity in this case. At the same time, there is an infinite number of combinations (β, φ) satisfying the considered relative configuration of the modules.

Angles α and β allow us to compute matrix $\mathbf{T}_2$ using Eq. (2). Next, we consider the position part of Eq. (3), from where we find vector $\mathbf{p}_{O_1}$:

$$\mathbf{p}_{O_1} = l_{OF}\hat{\mathbf{z}} + \mathbf{R}_z(\alpha)\mathbf{R}_x(\beta)\left(l_{FO_2}\hat{\mathbf{z}} + \mathbf{p}\right). \tag{6}$$

Thus, we have determined matrices $\mathbf{T}_1$ and $\mathbf{T}_2$ that specify configurations of the upper and lower modules relative to the base. We can now proceed with the independent analysis of each module and its mechanical constraints.

3.2. Constraints of the upper module

The mechanical constraints of the upper module are due to the limited displacements of its carriages and limited inclination angles of the rods in its spherical joints. Next, we discuss how to compute these displacements and inclination angles.

Let $i = 1, \ldots, 4$ be the branch number of the upper module, and let points A_i and B_i indicate the centers of the spherical joints in the i-th branch (Fig. 2a; for branches with the parallelogram sub-chains, we can select these points in the middle of the parallelogram short sides). Vectors $\mathbf{p}_{A_i}$ and $\mathbf{p}_{B_i}$ define the positions of these points in frame $Oxyz$:

$$\mathbf{p}_{A_i} = \begin{bmatrix} \boldsymbol{\rho}_{A_i} \\ h_i \end{bmatrix}, \qquad \begin{bmatrix} \mathbf{p}_{B_i} \\ 1 \end{bmatrix} = \mathbf{T}_1 \begin{bmatrix} \mathbf{r}_{B_i} \\ 1 \end{bmatrix}, \tag{7}$$

where h_i is the carriage displacement; vector $\boldsymbol{\rho}_{A_i}$ defines the x and y coordinates of point A_i in frame $Oxyz$; vector $\mathbf{r}_{B_i}$ defines the coordinates of point B_i in frame $O_1x_1y_1z_1$. Parameters $\boldsymbol{\rho}_{A_i}$ and $\mathbf{r}_{B_i}$ have constant values that depend on the robot geometry.

The distance between points A_i and B_i is constant and equal to rod length l_{AB}, which we assume is identical for each branch. Thus, we can write the following expression:

$$\|\mathbf{p}_{A_i} - \mathbf{p}_{B_i}\|^2 = l_{AB}^2. \tag{8}$$

https://doi.org/10.1017/S0263574725102592 Published online by Cambridge University Press

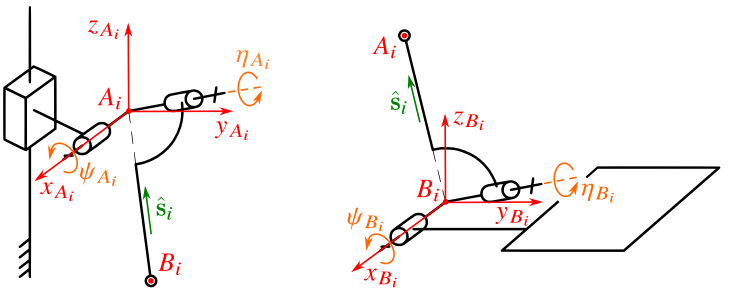


Fig. 3. *Equivalent representation of the spherical joints in the i-th branch of the upper module: (a) spherical joint of the carriage; (b) spherical joint of the moving platform.*

Substituting Eq. (7) into Eq. (8), we compute parameter h_i:

$$h_i = \pm\sqrt{l_{AB}^2 - \left(x_{B_i} - x_{A_i}\right)^2 - \left(y_{B_i} - y_{A_i}\right)^2} + z_{B_i}, \tag{9}$$

where $[x_{A_i}\ y_{A_i}]^{\mathrm{T}} = \boldsymbol{\rho}_{A_i}$ and $[x_{B_i}\ y_{B_i}\ z_{B_i}]^{\mathrm{T}} = \mathbf{p}_{B_i}$.

The $\pm$ sign in Eq. (9) corresponds to the carriage position above or below the moving platform. We select the plus sign for each branch according to the robot design. This design imposes the following constraints on the carriage displacement:

$$h_{\min} \le h_i \le h_{\max}, \tag{10}$$

where $h_{\min}$ and $h_{\max}$ are the minimum and maximum values of displacement h_i, which we assume identical for each branch.

Next, we consider the constraints on the rod inclination in the spherical joints. We start with the carriage spherical joint, centered at point A_i. To analyze how this joint constrains the rod motion, we represent the spherical joint as a combination of two revolute joints with intersecting and orthogonal axes (Fig. 3a). We ignore the third rotation of the rod (about line A_iB_i) because it does not affect the platform motion.

Let ψ_{A_i} and η_{A_i} be the rotational angles in these revolute joints. We introduce the $A_ix_{A_i}y_{A_i}z_{A_i}$ reference frame, whose axes $A_ix_{A_i}$ and $A_iy_{A_i}$ are parallel to the Oxy plane and coincident with the axes of the revolute joints when $\psi_{A_i} = \eta_{A_i} = 0$. Constant rotation matrix $\mathbf{R}_{A_i}$ determines the orientation of this frame relative to $Oxyz$. According to the robot design, we can write:

$$\mathbf{R}_{A_1} = \mathbf{R}_z(\pi/2), \qquad \mathbf{R}_{A_2} = \mathbf{R}_{A_3} = \mathbf{I}_3, \qquad \mathbf{R}_{A_4} = \mathbf{R}_z(-\pi/2). \tag{11}$$

Let $\hat{\mathbf{s}}_i$ be a unit vector directed from point B_i to point A_i, expressed in the $Oxyz$ frame. Figure 3a shows that this vector depends on angles ψ_{A_i} and η_{A_i} by the following equation:

$$\hat{\mathbf{s}}_i = \mathbf{R}_{A_i}\mathbf{R}_x(\psi_{A_i})\mathbf{R}_y(\eta_{A_i})\hat{\mathbf{z}}, \tag{12}$$

which we rewrite as below:

$$\mathbf{R}_{A_i}^{\mathrm{T}}\hat{\mathbf{s}}_i = \mathbf{R}_x(\psi_{A_i})\mathbf{R}_y(\eta_{A_i})\hat{\mathbf{z}} = \begin{bmatrix} \sin(\eta_{A_i}) \\ -\sin(\psi_{A_i})\cos(\eta_{A_i}) \\ \cos(\psi_{A_i})\cos(\eta_{A_i}) \end{bmatrix}. \tag{13}$$

The left side of Eq. (13) is known because vector $\hat{\mathbf{s}}_i = (\mathbf{p}_{A_i} - \mathbf{p}_{B_i})/l_{AB}$, and it can be computed using Eq. (7). Let $\mathbf{R}_{A_i}^{\mathrm{T}}\hat{\mathbf{s}}_i = [s_i^x\ s_i^y\ s_i^z]^{\mathrm{T}}$, then we can find the angles using the following expressions:

$$\psi_{A_i} = \operatorname{atan2}(-s_i^y, s_i^z), \qquad \eta_{A_i} = \operatorname{asin}(s_i^x), \tag{14}$$

which are valid because $|\eta_{A_i}|$ is usually much less than 90° in physical spherical joints.

https://doi.org/10.1017/S0263574725102592 Published online by Cambridge University Press

Angles ψ_{A_i} and η_{A_i} are limited by the robot design:

$$\psi_{A\min} \le \psi_{A_i} \le \psi_{A\max}, \qquad \eta_{A\min} \le \eta_{A_i} \le \eta_{A\max}, \tag{15}$$

where $\psi_{A\min}$, $\eta_{A\min}$, $\psi_{A\max}$, and $\eta_{A\max}$ are the minimum and maximum values of angles ψ_{A_i} and η_{A_i}, and we assume the minimum and maximum values are identical for each branch.

Constraints in the spherical joints of the moving platform are analyzed in the same way. We represent the spherical joint in the i-th branch as a combination of two revolute joints, whose axes intersect orthogonally at point B_i (Fig. 3b). Let ψ_{B_i} and η_{B_i} be the rotational angles in these revolute joints. We define the $B_i x_{B_i} y_{B_i} z_{B_i}$ reference frame, whose axes $B_i x_{B_i}$ and $B_i y_{B_i}$ are parallel to the $O_1 x_1 y_1$ plane and coincident with the axes of the revolute joints when $\psi_{B_i} = \eta_{B_i} = 0$. Constant rotation matrix $\mathbf{R}_{B_i}$ determines the orientation of this frame relative to $O_1 x_1 y_1$. We place each frame $B_i x_{B_i} y_{B_i} z_{B_i}$ in such a way that $\mathbf{R}_{B_i} = \mathbf{R}_{A_i}$ for each $i = 1, \ldots, 4$.

To find angles ψ_{B_i} and η_{B_i}, we follow the same approach as for the carriage spherical joint. We can compose an equation similar to Eq. (12). Its right side should include rotation matrix $\mathbf{R}_y(\varphi)$, which corresponds to the tilt of the upper platform. Therefore, we obtain the following expression:

$$\hat{\mathbf{s}}_i = \mathbf{R}_y(\varphi)\mathbf{R}_{B_i}\mathbf{R}_x(\psi_{B_i})\mathbf{R}_y(\eta_{B_i})\hat{\mathbf{z}}, \tag{16}$$

which we rewrite as below:

$$\mathbf{R}_{B_i}^{\mathrm{T}}\mathbf{R}_y^{\mathrm{T}}(\varphi)\hat{\mathbf{s}}_i = \mathbf{R}_x(\psi_{B_i})\mathbf{R}_y(\eta_{B_i})\hat{\mathbf{z}} = \begin{bmatrix} \sin(\eta_{B_i}) \\ -\sin(\psi_{B_i})\cos(\eta_{B_i}) \\ \cos(\psi_{B_i})\cos(\eta_{B_i}) \end{bmatrix}. \tag{17}$$

The right side of Eq. (17) is similar to Eq. (13), and we compute angles ψ_{B_i} and η_{B_i} using expressions similar to Eq. (14). These angles are limited by the robot design:

$$\psi_{B\min} \le \psi_{B_i} \le \psi_{B\max}, \qquad \eta_{B\min} \le \eta_{B_i} \le \eta_{B\max}, \tag{18}$$

where $\psi_{B\min}$, $\eta_{B\min}$, $\psi_{B\max}$, and $\eta_{B\max}$ are the minimum and maximum values of angles ψ_{B_i} and η_{B_i}, and we assume the minimum and maximum values are identical for each branch.

Thus, we have analyzed all mechanical constraints of the upper module. Before proceeding to the lower module, we should make a couple of remarks about the performed analysis:

1. To analyze the constraints in the spherical joints, we represent each joint as a combination of two revolute joints with intersecting and orthogonal axes. This representation is not unique. For example, in Fig. 3a, we could assume that the axis of the second revolute joint coincides with the $A_i z_{A_i}$ axis when $\psi_{A_i} = 0$, instead of the $A_i y_{A_i}$ axis. In this case, multiplier $\mathbf{R}_y(\eta_{A_i})\hat{\mathbf{z}}$ in the right side of Eq. (12) should be replaced with $-\mathbf{R}_z(\eta_{A_i})\hat{\mathbf{y}}$. Equations (13) and (14) change too, as well as limits $\psi_{A\min}$ and $\psi_{A\max}$ in Eq. (15).
2. The branches with the parallelogram sub-chains include two rods ending with the spherical joints. Each rod in such a parallelogram sub-chain inclines by the same angles. Therefore, angles ψ_{A_i}, η_{A_i}, ψ_{B_i}, and η_{B_i} in these branches are computed correctly with our assumption that points A_i are B_i are the middle points of the short sides of the parallelograms.

3.3. Constraints of the lower module

The mechanical constraints of the lower module include the limited rotational angles in its revolute joints and the possible collision of its carriages. Next, we show how to find these angles and check the collision.

We start with the central branch that has two revolute joints (Fig. 2b). Angle α in the first joint is not constrained: the lower moving platform can rotate unlimitedly about the axis of the circular rail. On the other hand, angle β is limited by the robot design:

$$\beta_{\min} \le \beta \le \beta_{\max}, \tag{19}$$

where $\beta_{\min}$ and $\beta_{\max}$ are the minimum and maximum values of angle β.

https://doi.org/10.1017/S0263574725102592 Published online by Cambridge University Press

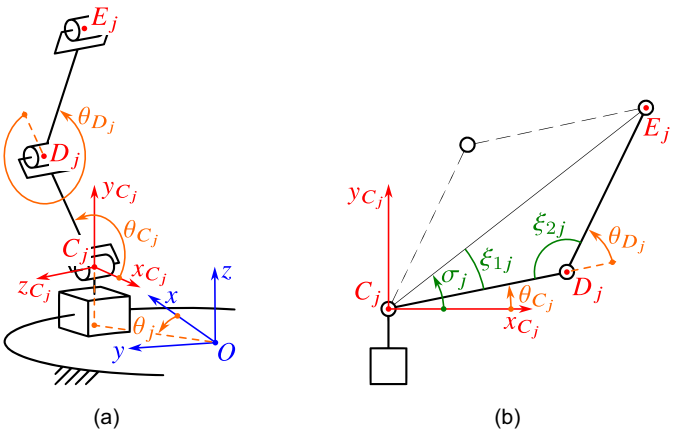


Fig. 4. *Rotational angles in the joints of the j-th lateral branch of the lower module: (a) location of frame $C_j x_{C_j} y_{C_j} z_{C_j}$; (b) planar view of the j-th branch.*

Next, we consider the lateral branches of the lower module. Let $j = 1, 2$ be the branch number. For the j-th branch, we define three points, C_j, D_j, and E_j, as follows. Point E_j is the intersection of the axes of the two revolute joints near the moving platform. Points C_j and D_j stay in the vertical plane passing through point E_j and belong to the axes of two other revolute joints, as shown in Figs. 2b and 4.

Vectors $\mathbf{p}_{C_j}$ and $\mathbf{p}_{E_j}$ define the positions of points C_j and E_j in frame $Oxyz$:

$$\mathbf{p}_{C_j} = \begin{bmatrix} R_C \cos(\theta_j) \\ R_C \sin(\theta_j) \\ z_C \end{bmatrix}, \qquad \begin{bmatrix} \mathbf{p}_{E_j} \\ 1 \end{bmatrix} = \mathbf{T}_2 \begin{bmatrix} \mathbf{r}_{E_j} \\ 1 \end{bmatrix}, \tag{20}$$

where θ_j is the carriage angular displacement; parameters R_C and z_C define the radial and vertical position of point C_j in frame $Oxyz$, and we assume these parameters are identical for each branch; vector $\mathbf{r}_{E_j}$ defines the coordinates of point E_j in frame $O_2 x_2 y_2 z_2$. Parameters R_C, z_C, and $\mathbf{r}_{E_j}$ have constant values that depend on the robot geometry.

Points C_j and E_j belong to the same vertical plane; therefore, we can compute angle θ_j as follows:

$$\theta_j = \operatorname{atan2}(y_{E_j}, x_{E_j}), \tag{21}$$

where x_{E_j} and y_{E_j} are the first two components of vector $\mathbf{p}_{E_j}$.

To avoid the collision of the carriages, we should limit angles θ_j. Let $\theta_{\min} > 0$ be the minimum angular distance between the carriages, which is defined by the robot design. Since the image of the atan2 function in Eq. (21) is $[-\pi, \pi]$, the following inequalities ensure that the carriages do not collide:

$$\theta_{\min} \le |\theta_1 - \theta_2| \le 2\pi - \theta_{\min}. \tag{22}$$

Next, we analyze the constraints in two revolute joints, whose axes pass through points C_j and D_j. Let θ_{C_j} and θ_{D_j} be the rotational angles in these joints (Fig. 4a). To find these angles, we first introduce reference frame $C_j x_{C_j} y_{C_j} z_{C_j}$ attached to the j-th carriage. Its axis $C_j y_{C_j}$ is parallel to the Oz axis, and axis $C_j x_{C_j}$ is opposite to the Ox axis when $\theta_j = 0$. Rotation matrix $\mathbf{R}_{C_j}$ defines the orientation of this frame relative to $Oxyz$ and can be written as follows:

$$\mathbf{R}_{C_j} = \left[-\mathbf{R}_z(\theta_j)\hat{\mathbf{x}} \quad \hat{\mathbf{z}} \quad \hat{\mathbf{z}} \times \left(\mathbf{R}_z(\theta_j)\hat{\mathbf{x}} \right) \right] = \begin{bmatrix} -\cos(\theta_j) & 0 & -\sin(\theta_j) \\ -\sin(\theta_j) & 0 & \cos(\theta_j) \\ 0 & 1 & 0 \end{bmatrix}, \tag{23}$$

https://doi.org/10.1017/S0263574725102592 Published online by Cambridge University Press

and transformation matrix $\mathbf{T}_{C_j}$ between frames $C_j x_{C_j} y_{C_j} z_{C_j}$ and $Oxyz$ has the following form:

$$\mathbf{T}_{C_j} = \begin{bmatrix} \mathbf{R}_{C_j} & \mathbf{p}_{C_j} \\ \mathbf{0}^{\mathrm{T}} & 1 \end{bmatrix}. \tag{24}$$

Matrix $\mathbf{T}_{C_j}$ depends only on angle θ_j, which we computed in Eq. (21). Now, we can consider the 2-DOF planar mechanism located in plane $C_j x_{C_j} y_{C_j}$ (Fig. 4b). Let $\boldsymbol{\rho}_{E_j} = [x_j \; y_j]^{\mathrm{T}}$ be the position vector of point E_j in frame $C_j x_{C_j} y_{C_j}$. This vector is related to vector $\mathbf{p}_{E_j}$ by transformation matrix $\mathbf{T}_{C_j}$:

$$\begin{bmatrix} \mathbf{p}_{E_j} \\ 1 \end{bmatrix} = \mathbf{T}_{C_j} \begin{bmatrix} \boldsymbol{\rho}_{E_j} \\ 0 \\ 1 \end{bmatrix}, \tag{25}$$

from where we determine vector $\boldsymbol{\rho}_{E_j}$:

$$\begin{bmatrix} \boldsymbol{\rho}_{E_j} \\ 0 \\ 1 \end{bmatrix} = \mathbf{T}_{C_j}^{-1} \begin{bmatrix} \mathbf{p}_{E_j} \\ 1 \end{bmatrix} = \begin{bmatrix} \mathbf{R}_{C_j}^{\mathrm{T}} & -\mathbf{R}_{C_j}^{\mathrm{T}} \mathbf{p}_{C_j} \\ \mathbf{0}^{\mathrm{T}} & 1 \end{bmatrix} \begin{bmatrix} \mathbf{p}_{E_j} \\ 1 \end{bmatrix}. \tag{26}$$

To compute angles θ_{C_j} and θ_{D_j}, we follow the approach from [51, sect. 6] and introduce three auxiliary angles, σ_j, ξ_{1j}, and ξ_{2j} (Fig. 4b), which can be found from the following expressions:

$$\sigma_j = \operatorname{atan2}(y_j, x_j), \;\; \xi_{1j} = \operatorname{acos}\left(\frac{\|\boldsymbol{\rho}_{E_j}\|^2 + l_{CD}^2 - l_{DE}^2}{2\|\boldsymbol{\rho}_{E_j}\| l_{CD}} \right), \;\; \xi_{2j} = \operatorname{acos}\left(\frac{l_{CD}^2 + l_{DE}^2 - \|\boldsymbol{\rho}_{E_j}\|^2}{2 l_{CD} l_{DE}} \right), \tag{27}$$

where l_{CD} and l_{DE} are the lengths of links $C_j D_j$ and $D_j E_j$, respectively, which we assume identical for each branch.

Using these angles, we determine two sets of solutions for angles θ_{C_j} and θ_{D_j}:

$$\begin{aligned} \theta_{C_j} &= \sigma_j - \xi_{1j}, \\ \theta_{D_j} &= \pi - \xi_{2j}, \end{aligned} \quad \text{and} \quad \begin{aligned} \theta_{C_j} &= \sigma_j + \xi_{1j}, \\ \theta_{D_j} &= \xi_{2j} - \pi. \end{aligned} \tag{28}$$

The first solution set matches the "elbow-down" case when $\theta_{D_j} > 0$; the second solution set matches the "elbow-up" case when $\theta_{D_j} < 0$. We choose the second set according to the lower module design (Fig. 1). This design imposes the following constraints on angles θ_{C_j} and θ_{D_j}:

$$\theta_{C\min} \le \theta_{C_j} \le \theta_{C\max}, \qquad \theta_{D\min} \le \theta_{D_j} \le \theta_{D\max}, \tag{29}$$

where $\theta_{C\min}$, $\theta_{D\min}$, $\theta_{C\max}$, and $\theta_{D\max}$ are the minimum and maximum values of angles θ_{C_j} and θ_{D_j}, and we assume the minimum and maximum values are identical for each branch.

Rotation in the revolute joint between the coupler and the moving platform is not constrained according to the robot design. Thus, it remains to check the rotational angle θ_{E_j} in the revolute joint whose axis passes through point E_j. We measure this angle as the angle between two unit vectors, $\hat{\mathbf{u}}_j$ and $\hat{\mathbf{v}}_j$, directed along line $D_j E_j$ and the axis of the platform revolute joint, respectively (Fig. 5). We compute these unit vectors using the following expressions:

$$\hat{\mathbf{u}}_j = \frac{\mathbf{p}_{E_j} - \mathbf{p}_{D_j}}{l_{DE}}, \qquad \begin{bmatrix} \hat{\mathbf{v}}_j \\ 0 \end{bmatrix} = \mathbf{T}_2 \begin{bmatrix} \hat{\mathbf{e}}_j \\ 0 \end{bmatrix}, \tag{30}$$

where $\mathbf{p}_{D_j}$ is the position vector of point D_j in frame $Oxyz$; $\hat{\mathbf{e}}_j$ is a unit vector along the axis of the platform revolute joint, expressed in frame $O_2 x_2 y_2 z_2$. Vector $\hat{\mathbf{e}}_j$ is constant and defined by the geometry of the lower module. Vector $\mathbf{p}_{D_j}$ can be computed similarly to Eq. (25), where we replace vector $\boldsymbol{\rho}_{E_j}$ with vector $\boldsymbol{\rho}_{D_j} = [l_{CD} \cos(\theta_{C_j}) \;\; l_{CD} \sin(\theta_{C_j})]^{\mathrm{T}}$.

To set the constraints on angle θ_{E_j} correctly, we must ensure that it is measured in the same sense, disregarding the directions of vectors $\hat{\mathbf{u}}_j$ and $\hat{\mathbf{v}}_j$. For this purpose, we introduce two auxiliary vectors.

https://doi.org/10.1017/S0263574725102592 Published online by Cambridge University Press

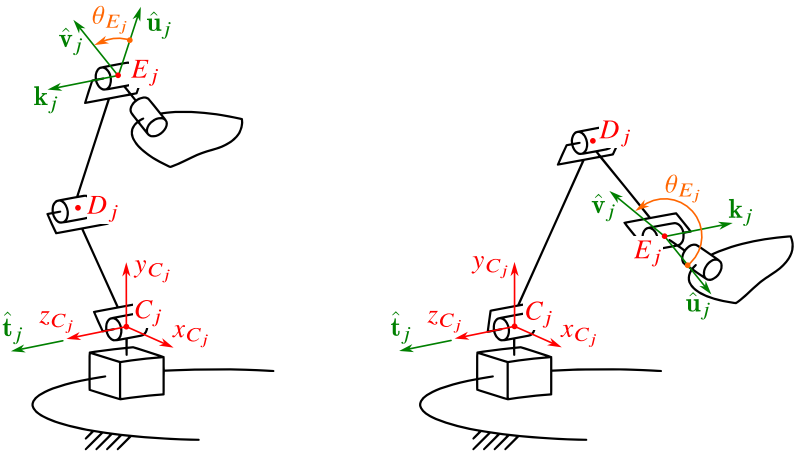


Fig. 5. *Measuring angle θ_{E_j}: (a) vectors $\mathbf{k}_j$ and $\hat{\mathbf{t}}_j$ have the same directions; (a) vectors $\mathbf{k}_j$ and $\hat{\mathbf{t}}_j$ have opposite directions.*

The first one is $\mathbf{k}_j = \hat{\mathbf{u}}_j \times \hat{\mathbf{v}}_j$, which is orthogonal to both vectors $\hat{\mathbf{u}}_j$ and $\hat{\mathbf{v}}_j$. The second auxiliary vector is $\hat{\mathbf{t}}_j$ parallel to the $C_j z_j$ axis and equal to the third column of rotation matrix $\mathbf{R}_{C_j}$ in Eq. (23) (Fig. 5). Using these vectors, we can compute angle θ_{E_j} as follows:

$$\theta_{E_j} = \begin{cases} \operatorname{acos}(\hat{\mathbf{u}}_j \cdot \hat{\mathbf{v}}_j), & \text{if} \quad \mathbf{k}_j \cdot \hat{\mathbf{t}}_j \geq 0, \\ 2\pi - \operatorname{acos}(\hat{\mathbf{u}}_j \cdot \hat{\mathbf{v}}_j), & \text{if} \quad \mathbf{k}_j \cdot \hat{\mathbf{t}}_j < 0. \end{cases} \tag{31}$$

In the first case, vectors $\mathbf{k}_j$ and $\hat{\mathbf{t}}_j$ have the same directions, and angle $\theta_{E_j} \in [0°, 180°]$ (Fig. 5a). In the second case, vectors $\mathbf{k}_j$ and $\hat{\mathbf{t}}_j$ have opposite directions, and angle $\theta_{E_j} \in (180°, 360°)$ (Fig. 5b). We can now define the constraints on angle θ_{E_j}:

$$\theta_{E\min} \leq \theta_{E_j} \leq \theta_{E\max}, \tag{32}$$

where $\theta_{E\min}$ and $\theta_{E\max}$ are the minimum and maximum values of angle θ_{E_j}, and we assume the minimum and maximum values are identical for each branch. This concludes the analysis of the mechanical constraints of the lower module.

3.4. Interference between the upper and lower modules

Satisfying the mechanical constraints considered in Sections 3.2 and 3.3 does not guarantee that the upper and lower modules will not interfere with each other. This interference includes collisions between the links of the modules. It affects the workspace of the hybrid robot and should be checked for correct workspace evaluation.

The collision detection problem of the robot links relates directly to analyzing collisions between the rigid bodies representing these links. There are various techniques developed to solve this problem [52, 53]. In this paper, we apply the familiar Gilbert–Johnson–Keerthi (GJK) algorithm [54]. This computationally efficient algorithm allows us to find the distance between convex bodies and, therefore, to check whether they collide or not. The major idea of the GJK algorithm relies on computing the Minkowski difference of two convex subsets of the Euclidean space and evaluating support functions over this difference – we omit the mathematical foundations here, which can be found in the original paper and elsewhere [55–57]. Next, we show how to adapt this algorithm to the considered hybrid robot.

https://doi.org/10.1017/S0263574725102592 Published online by Cambridge University Press

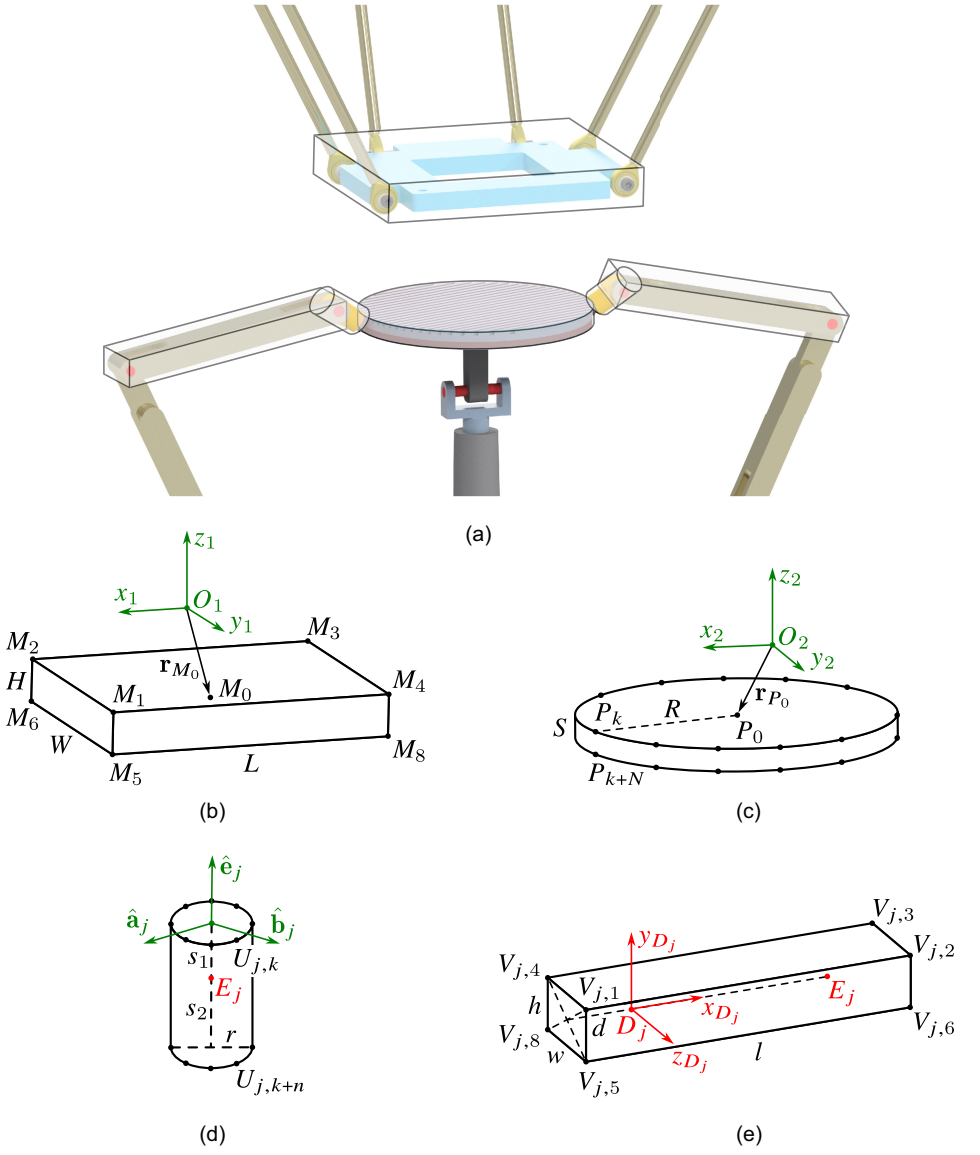


Fig. 6. *Collision analysis of the upper and lower modules: (a) convex bodies enveloping the links that can collide; (b) parallelepiped around the upper platform; (c) cylinder around the lower platform; (d) cylinder around the j-th coupler; (e) parallelepiped around the j-th upper bar.*

According to the robot design (Fig. 1), its upper moving platform should operate above the lower moving platform. Therefore, we consider the following collisions, which are possible between the links of the modules (Fig. 6a):

1. Collision between the upper platform and the lower platform.
2. Collision between the upper platform and the couplers of the lower module.
3. Collision between the upper platform and the upper bars of the lower module.

In this paper, we follow the original GJK algorithm [54], where the analyzed rigid bodies are not arbitrary convex objects but convex polytopes. Thus, we should represent each link mentioned above as a convex polytope. The following sections describe this representation.

https://doi.org/10.1017/S0263574725102592 Published online by Cambridge University Press

3.4.1. Upper platform

For the upper platform, we define a rectangular parallelepiped that envelops the moving platform and its spherical joints (Fig. 6b). The parallelepiped is determined by the coordinates of its vertices. Let M_0 be the parallelepiped center and M_k, $k = 1, \ldots, 8$, be its vertices, where $M_1, \ldots, M_4$ and $M_5, \ldots, M_8$ correspond to the top and bottom parallelepiped faces, respectively. We can write coordinates $\mathbf{r}_{M_k}$ of these points in frame $O_1x_1y_1z_1$:

$$\mathbf{r}_{M_k} = \mathbf{r}_{M_0} + \frac{1}{2}\begin{bmatrix} \varepsilon_k L \\ \delta_k W \\ \zeta_k H \end{bmatrix}, \tag{33}$$

$$\varepsilon_k = \begin{cases} 1, & \text{if} \quad k = 1, 2, 5, 6, \\ -1, & \text{if} \quad k = 3, 4, 7, 8, \end{cases} \quad \delta_k = \begin{cases} 1, & \text{if} \quad k = 1, 4, 5, 8, \\ -1, & \text{if} \quad k = 2, 3, 6, 7, \end{cases} \quad \zeta_k = \begin{cases} 1, & \text{if} \quad k = 1, 2, 3, 4, \\ -1, & \text{if} \quad k = 5, 6, 7, 8, \end{cases}$$

where $\mathbf{r}_{M_0}$ is the position vector of point M_0 in frame $O_1x_1y_1z_1$; L, W, and H are the length, width, and height of the parallelepiped. All these parameters have constant values depending on the robot design.

3.4.2. Lower platform

We represent the lower moving platform as a right circular cylinder with radius R and height S (Fig. 6c). To convert the cylinder into a convex polytope, we sample each circular boundary into N points. Let P_0 be the center of the top cylinder face and P_k, $k = 1, \ldots, 2N$, be the sample points, where $P_1, \ldots, P_N$ and $P_{N+1}, \ldots, P_{2N}$ correspond to the top and bottom cylinder faces, respectively. We can write coordinates $\mathbf{r}_{P_k}$ of these points in frame $O_2x_2y_2z_2$:

$$\mathbf{r}_{P_k} = \begin{cases} \mathbf{r}_{P_0} + \begin{bmatrix} R\cos(2\pi(k-1)/N) \\ R\sin(2\pi(k-1)/N) \\ 0 \end{bmatrix}, & \text{if} \quad k = 1, \ldots, N, \\ \mathbf{r}_{P_{k-N}} - S\hat{\mathbf{z}}, & \text{if} \quad k = N+1, \ldots, 2N, \end{cases} \tag{34}$$

where $\mathbf{r}_{P_0}$ is the position vector of point P_0 in frame $O_2x_2y_2z_2$. Parameters R, S, and $\mathbf{r}_{P_0}$ depend on the platform design and have known and constant values.

3.4.3. Couplers

We also use a right circular cylinder to represent each coupler (Fig. 6d). According to the robot design and Section 3.3, the axis of the j-th cylinder, $j = 1, 2$, passes through point E_j with coordinates $\mathbf{r}_{E_j}$, and it is directed along vector $\hat{\mathbf{e}}_j$ (in frame $O_2x_2y_2z_2$). Let r be the cylinder radius and s_1 and s_2 be the distances from point E_j to the top and bottom cylinder faces, respectively. Because the cylinder is symmetrical above its axis, we can ignore the coupler rotation relative to the moving platform. Therefore, parameters $\mathbf{r}_{E_j}$, $\hat{\mathbf{e}}_j$, r, s_1, and s_2 fully define the cylinder geometry in frame $O_2x_2y_2z_2$. All these parameters have known values depending on the robot design.

To convert the cylinder into a convex polytope, we follow the same approach and sample each circular boundary into n points. Let $U_{j,k}$, $k = 1, \ldots, 2n$, be the sample points, where $U_{j,1}, \ldots, U_{j,n}$ and $U_{j,n+1}, \ldots, U_{j,2n}$ correspond to the top and bottom faces of the j-th cylinder, respectively. These points have coordinates $\mathbf{r}_{U_{j,k}}$ in frame $O_2x_2y_2z_2$:

$$\mathbf{r}_{U_{j,k}} = \begin{cases} \mathbf{r}_{E_j} + s_1\hat{\mathbf{e}}_j + r(\cos(2\pi(k-1)/n)\hat{\mathbf{a}}_j + \sin(2\pi(k-1)/n)\hat{\mathbf{b}}_j), & \text{if} \quad k = 1, \ldots, n, \\ \mathbf{r}_{U_{j,k-n}} - (s_1 + s_2)\hat{\mathbf{e}}_j, & \text{if} \quad k = n+1, \ldots, 2n, \end{cases} \tag{35}$$

where $\hat{\mathbf{a}}_j$ and $\hat{\mathbf{b}}_j$ are two orthonormal vectors orthogonal to vector $\hat{\mathbf{e}}_j$, which can be found as follows:

$$\operatorname{span}\left(\{\hat{\mathbf{a}}_j, \hat{\mathbf{b}}_j\}\right) = \operatorname{null}\left(\hat{\mathbf{e}}_j^{\mathrm{T}}\right). \tag{36}$$

https://doi.org/10.1017/S0263574725102592 Published online by Cambridge University Press

Equations (33)–(35) are sufficient to analyze the collisions between the upper platform, the lower platform, and the couplers. For this purpose, we just need to transform coordinates $\mathbf{r}_{M_k}$ from frame $O_1x_1y_1z_1$ to frame $O_2x_2y_2z_2$ using transformation matrix $\mathbf{T}$. Thus, these collisions are analyzed in frame $O_2x_2y_2z_2$ with no need to transform coordinates $\mathbf{r}_{P_k}$ and $\mathbf{r}_{U_{j,k}}$.

3.4.4. Upper bars

Finally, we use a rectangular parallelepiped to represent the geometry of each upper bar (Fig. 6e). Let $V_{j,k}$, $k = 1, \ldots, 8$, be its vertices, where $V_{j,1}, \ldots, V_{j,4}$ and $V_{j,5}, \ldots, V_{j,8}$ correspond to the top and bottom faces of the j-th parallelepiped, respectively ($j = 1, 2$). To find the coordinates of these vertices, we first introduce reference frame $D_jx_{D_j}y_{D_j}z_{D_j}$ attached to the j-th upper bar. Its $D_jx_{D_j}$ axis coincides with line D_jE_j, and the $D_jz_{D_j}$ axis has the same direction as axis $C_jz_{C_j}$. We can write coordinates $\mathbf{r}_{V_{j,k}}$ of the parallelepiped vertices in frame $D_jx_{D_j}y_{D_j}z_{D_j}$:

$$\mathbf{r}_{V_{j,k}} = \begin{cases} \begin{bmatrix} -d \\ \zeta_k h/2 \\ \varepsilon_k w/2 \end{bmatrix}, & \text{if} \quad k = 1, 4, 5, 8, \\ \mathbf{r}_{V_{j,k-4}} + l\hat{\mathbf{x}}, & \text{if} \quad k = 2, 3, 6, 7, \end{cases} \tag{37}$$

where l, w, and h are the length, width, and height of the parallelepiped; d is a distance from point D_j to the left face of the parallelepiped; ζ_k and ε_k have the same meaning as in Eq. (33). All these parameters have constant values depending on the robot design.

To analyze the collision between the upper platform and the j-th upper bar, we should express coordinates $\mathbf{r}_{M_k}$ and $\mathbf{r}_{V_{j,k}}$ in the same reference frame, for example, in base frame $Oxyz$. Let $\mathbf{p}_{M_k}$ and $\mathbf{p}_{V_{j,k}}$ denote these coordinates in this frame. We can compute these coordinates using transformation matrices $\mathbf{T}_1$ and $\mathbf{T}_{D_j}$:

$$\begin{bmatrix} \mathbf{p}_{M_k} \\ 1 \end{bmatrix} = \mathbf{T}_1 \begin{bmatrix} \mathbf{r}_{M_k} \\ 1 \end{bmatrix}, \qquad \begin{bmatrix} \mathbf{p}_{V_{j,k}} \\ 1 \end{bmatrix} = \mathbf{T}_{D_j} \begin{bmatrix} \mathbf{r}_{V_{j,k}} \\ 1 \end{bmatrix}, \tag{38}$$

where $\mathbf{T}_{D_j}$ is a transformation matrix between frames $D_jx_{D_j}y_{D_j}z_{D_j}$ and $Oxyz$:

$$\mathbf{T}_{D_j} = \mathbf{T}_{C_j} \begin{bmatrix} \mathbf{R}_z(\theta_{C_j}) & \mathbf{0} \\ \mathbf{0}^{\mathrm{T}} & 1 \end{bmatrix} \begin{bmatrix} \mathbf{I}_3 & l_{DE}\hat{\mathbf{x}} \\ \mathbf{0}^{\mathrm{T}} & 1 \end{bmatrix} \begin{bmatrix} \mathbf{R}_z(\theta_{D_j}) & \mathbf{0} \\ \mathbf{0}^{\mathrm{T}} & 1 \end{bmatrix}. \tag{39}$$

Thus, we have represented all the considered links as convex polytopes and derived the explicit expressions for the coordinates of their vertices. This information is sufficient to implement the GJK algorithm and check if the links collide. This concludes the workspace analysis of the hybrid robot. The next section considers numerical examples.

4. Examples

In this section, we consider two types of workspaces common to robotic systems [58, ch. 7]:

1. Translation workspace – the set of reachable positions of the upper moving platform relative to the lower moving platform when their relative orientation is fixed. In other words, we determine the set of position vectors $\mathbf{p}$ when rotation matrix $\mathbf{R}$ is constant.
2. Orientation workspace – the set of reachable orientations of the upper moving platform relative to the lower moving platform when their relative position is fixed. In other words, we determine the set of rotation matrices $\mathbf{R}$ when position vector $\mathbf{p}$ is constant.

https://doi.org/10.1017/S0263574725102592 Published online by Cambridge University Press

To make our analysis and representation of the results clearer, we parameterize rotation matrix $\mathbf{R}$ using tilt-and-torsion angles [50, 59]:

$$\mathbf{R} = \mathbf{R}_z(\psi)\mathbf{R}_y(\theta)\mathbf{R}_z(\sigma - \psi), \tag{40}$$

where ψ, θ, and σ are the azimuth, tilt, and torsion angles, respectively.

Here, angle θ characterizes the tilt of the upper platform relative to the lower one, while angle ψ determines the direction of this tilt. Finally, angle σ describes the self-rotation (torsion). We refer to paper [59] for more details about this parameterization and its advantages.

Geometrical parameters of the hybrid robot correspond to its computer model (Fig. 1) and have the following values:

- Upper module:

$$\boldsymbol{\rho}_{A_1} = \begin{bmatrix} 256 \\ 0 \end{bmatrix} \text{mm}, \quad \boldsymbol{\rho}_{A_2} = \begin{bmatrix} 50 \\ -256 \end{bmatrix} \text{mm}, \quad \boldsymbol{\rho}_{A_3} = \begin{bmatrix} -50 \\ -256 \end{bmatrix} \text{mm}, \quad \boldsymbol{\rho}_{A_4} = \begin{bmatrix} -256 \\ 0 \end{bmatrix} \text{mm},$$

$$\mathbf{r}_{B_1} = \begin{bmatrix} 84.5 \\ 0 \\ -6 \end{bmatrix} \text{mm}, \ \mathbf{r}_{B_2} = \begin{bmatrix} 50 \\ -84.5 \\ -6 \end{bmatrix} \text{mm}, \ \mathbf{r}_{B_3} = \begin{bmatrix} -50 \\ -84.5 \\ -6 \end{bmatrix} \text{mm}, \ \mathbf{r}_{B_4} = \begin{bmatrix} -84.5 \\ 0 \\ -6 \end{bmatrix} \text{mm},$$

$$l_{AB} = 379 \text{ mm}.$$

- Lower module:

$$l_{OF} = 204 \text{ mm}, \quad l_{FO_2} = 57.7 \text{ mm}, \quad R_C = 183.7 \text{ mm}, \quad z_C = 100.3 \text{ mm}, \quad l_{CD} = l_{DE} = 150 \text{ mm},$$

$$\mathbf{r}_{E_1} = \begin{bmatrix} 100.5 \\ 0 \\ 5.9 \end{bmatrix} \text{mm}, \quad \mathbf{r}_{E_2} = \begin{bmatrix} -100.5 \\ 0 \\ 5.9 \end{bmatrix} \text{mm}, \quad \hat{\mathbf{e}}_1 = \mathbf{R}_y(-32.2^\circ)\hat{\mathbf{x}}, \quad \hat{\mathbf{e}}_2 = \mathbf{R}_y(212.2^\circ)\hat{\mathbf{x}}.$$

Joints constraints of the lower and upper modules are listed below:

- Upper module:

$$h_{\min} = 490 \text{ mm}, \quad h_{\max} = 930 \text{ mm},$$

$$\psi_{A\min} = \psi_{B\min} = 0^\circ, \ \psi_{A\max} = \psi_{B\max} = 180^\circ, \ \eta_{A\min} = \eta_{B\min} = -20^\circ, \ \eta_{A\max} = \eta_{B\max} = 20^\circ.$$

- Lower module:

$$\beta_{\min} = -70^\circ, \quad \beta_{\max} = 70^\circ, \quad \theta_{\min} = 8^\circ,$$

$$\theta_{C\min} = -5^\circ, \ \theta_{C\max} = 180^\circ, \ \theta_{D\min} = -160^\circ, \ \theta_{D\max} = 160^\circ, \ \theta_{E\min} = 20^\circ, \ \theta_{E\max} = 340^\circ.$$

Finally, the parameters of the links for which we analyze the collisions are the following:

- Upper moving platform:

$$\mathbf{r}_{M_0} = \begin{bmatrix} 0 \\ -12.3 \\ -5 \end{bmatrix} \text{mm}, \quad L = 189 \text{ mm}, \quad W = 164 \text{ mm}, \quad H = 22 \text{ mm}.$$

- Lower moving platform:

$$\mathbf{r}_{P_0} = \begin{bmatrix} 0 \\ 0 \\ 0 \end{bmatrix} \text{mm}, \quad R = 78.7 \text{ mm}, \quad S = 13.1 \text{ mm}, \quad N = 12.$$

- Couplers:

$$r = 10.2 \text{ mm}, \quad s_1 = 0 \text{ mm}, \quad s_2 = 28.1 \text{ mm}, \quad n = 12.$$

https://doi.org/10.1017/S0263574725102592 Published online by Cambridge University Press

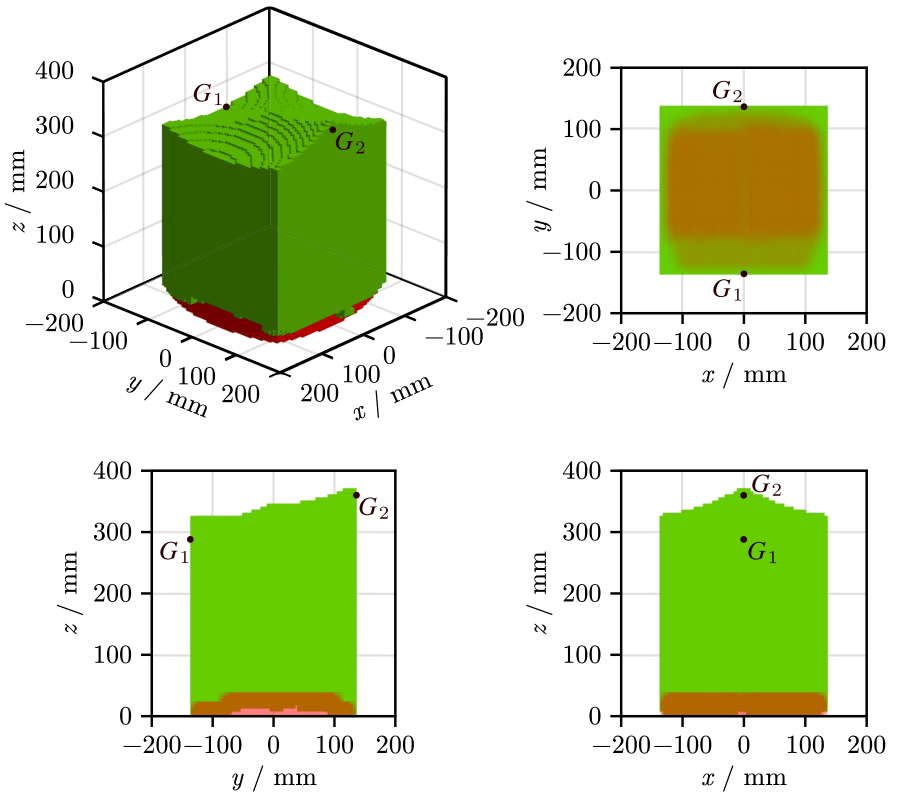


Fig. 7. *Translation workspace and its projections for $\psi = \theta = \sigma = 0°$.*

- Upper bars:

$$d = 7.9 \text{ mm}, \quad l = 2d + l_{DE} = 165.8 \text{ mm}, \quad w = 28.1 \text{ mm}, \quad h = 15.7 \text{ mm}.$$

All subsequent simulations have been performed in Julia [60]: the source code of the developed program is available at the link at the end of the paper. The GJK algorithm has been implemented using Julia package `EnhancedGJK.jl`.[1]

In the simulations, we first checked the joint constraints and then analyzed the link interference. The figures in the following sections present the results. In all the figures, green areas represent the resulting workspace that satisfies all constraints, while red areas indicate workspace points that meet the joint constraints but violate the collision constraints.

4.1. Translation workspace

To analyze the translation workspace, we sample the x, y, and z components of position vector $\mathbf{p}$ in ranges $[-200, 200]$ mm, $[-250, 250]$ mm, and $[0, 400]$ mm, respectively, with a step size of 5 mm for each component. In the first example, we consider the zero relative orientation of the modules: $\psi = \theta = \sigma = 0°$. Figure 7 shows the results. The translation workspace has a symmetrical shape that meets the symmetrical design of the robot. The workspace envelops the rectangular parallelepiped with the sides of 250 mm, 250 mm, and 300 mm along the x, y, and z directions, respectively. Note how the lower part of the analyzed space ($z < 30$ mm) is discarded because of the link interference.

[1] https://github.com/JuliaRobotics/EnhancedGJK.jl

https://doi.org/10.1017/S0263574725102592 Published online by Cambridge University Press

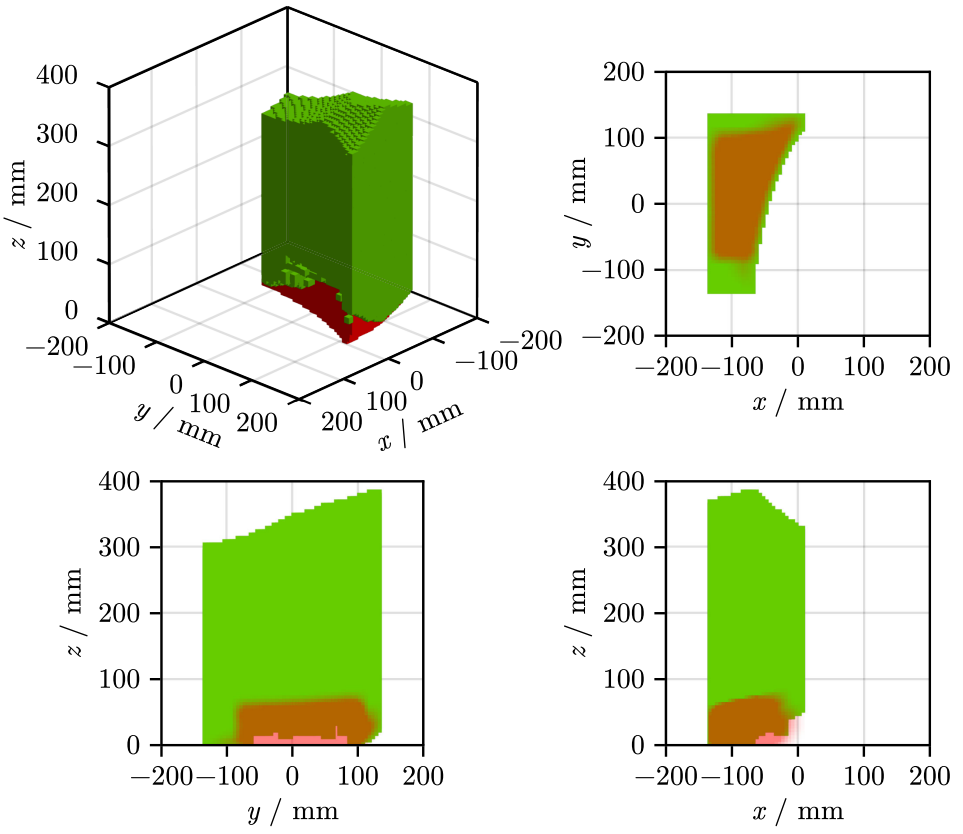


Fig. 8. *Translation workspace and its projections for* $\psi = 0°$, $\theta = -30°$, $\sigma = 0°$.

The second example considers the tilted configuration: $\psi = 0°$, $\theta = -30°$, $\sigma = 0°$. In this case, the upper platform tilts about the O_2y_2 axis, while the lower platform keeps zero orientation according to the robot design. Figure 8 shows that the workspace has been reduced by more than a half, and the points with $x > 0$ mm are unreachable with this orientation. The points with $z < 75$ mm are also unreachable because of the link interference between the modules.

In the third example, we consider the same tilt angle but alter the direction of the tilt axis: $\psi = 30°$, $\theta = -30°$, $\sigma = 0°$. Now, both the upper and lower moving platforms should rotate to achieve this relative orientation. The results in Fig. 9 look similar to Fig. 8, but the whole workspace becomes inclined, reflecting the changes of the tilt axis.

Finally, we add the non-zero torsion to the previous example: $\psi = 30°$, $\theta = -30°$, $\sigma = 45°$. Figure 10 shows the computed translation workspace. Although the workspace still has a large size in the z direction (about 300 mm), it has an irregular shape and is quite limited in the x and y directions, while the points with $x > 0$ mm remain unreachable.

4.2. Orientation workspace

To analyze the orientation workspace, we represent it in a polar coordinate system similar to paper [50]. For each considered value of torsion angle σ, we make a planar plot in polar axes where the radial coordinate is proportional to tilt angle θ and the angular coordinate is equal to azimuth angle ψ.

We specify all these angular parameters as follows. First, we sample tilt angle θ in range $[0°, 90°]$ with a step of 2.5°. Then, we sample azimuth angle ψ in range $[0°, 360°)$, and number p of its samples

https://doi.org/10.1017/S0263574725102592 Published online by Cambridge University Press

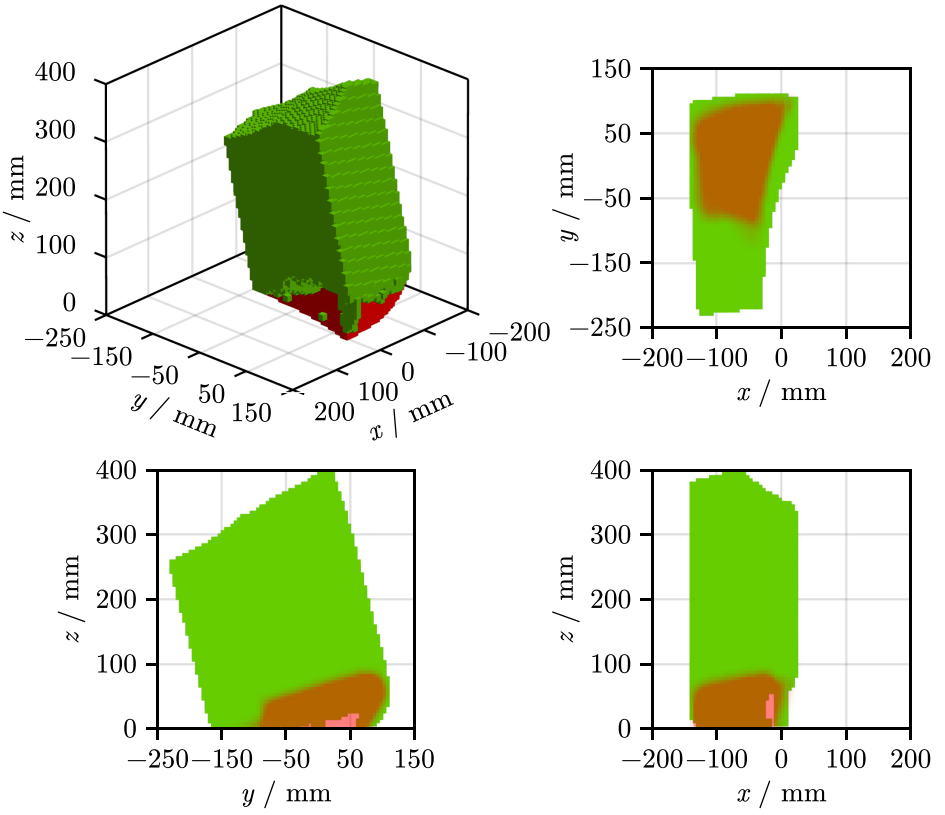


Fig. 9. *Translation workspace and its projections for* $\psi = 30°$, $\theta = -30°$, $\sigma = 0°$.

depends on the value of angle θ. If $\theta = 0°$, the azimuth angle is not defined, and we set $\psi = 0°$. If $\theta \neq 0°$, we compute number p as follows:

$$p = p_{\max} \left\lceil \frac{\theta}{\theta_{\max}} \right\rceil, \tag{41}$$

where $\theta_{\max}$ is the maximum considered value of angle θ, which is equal to 90° in our examples; $p_{\max}$ is a number of samples of angle ψ when $\theta = \theta_{\max}$, and we set $p_{\max} = 120$; $\lceil * \rceil$ is the ceiling function that gives the lowest integer greater or equal to its argument.

Equation (41) provides us with a uniform sampling of the polar coordinate space and avoids dense sampling near the origin, unlike the regular (independent) sampling of parameters ψ and θ. Finally, we consider four different values of torsion angle σ: 0°, 20°, 40°, and 60°.

In the first example, we examine the orientation workspace for the point near the geometric center of the translation workspace depicted in Fig. 7: $x = y = 0$ mm, $z = 150$ mm. Figure 11 illustrates the results. For each value of torsion angle σ, the upper platform can tilt relative to the lower platform for 20° in any direction. When azimuth angle ψ is near 90° or 270°, the upper platform can tilt further: tilt angle θ reaches 40° and even 60° with $\sigma = 40°$.

The second example considers the orientation workspace for the point at the same height but displaced along the x direction: $x = 100$ mm, $y = 0$ mm, $z = 150$ mm. Figure 12 shows that the upper platform can tilt only in a limited sector. For example, if we look at the plots for $\sigma = 0°$ and $\sigma = 20°$, we observe that tilt angle θ reaches 40° but the tilts are possible only for angles ψ in a range of about $[-90°, 90°]$. The orientation workspaces decreases as torsion angle σ takes higher values.

In the third example, we include the same displacement in the y direction: $x = 100$ mm, $y = 100$ mm, $z = 150$ mm. Figure 13 shows that the tilt sector (the range of angle ψ) decreases even more. The higher

https://doi.org/10.1017/S0263574725102592 Published online by Cambridge University Press

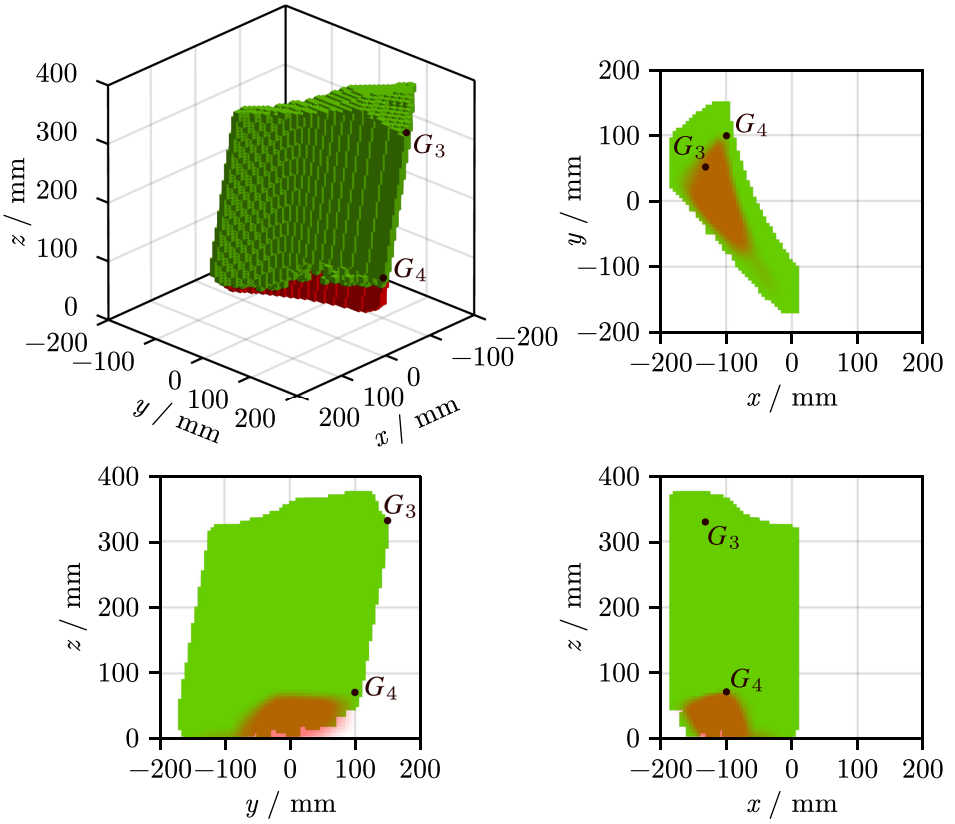


Fig. 10. *Translation workspace and its projections for $\psi = 30°$, $\theta = -30°$, $\sigma = 45°$.*

the torsion angle, the narrower this sector, but tilt angle θ can reach 60° for each considered value of angle σ.

The previous examples analyzed the orientation workspace when the upper platform stayed beyond the lower one, such that the links of the upper and lower modules did not interfere. In the fourth example, we consider the case when the platforms are near each other, and the height of the examined point is twice lower: $x = y = 0$ mm, $z = 75$ mm. Figure 14 illustrates the obtained orientation workspace. The regions of the link interference (the red areas in each plot) constrain the tilt angle: angle θ is limited by 40°, but it could reach 60° and even higher values if we ignore the link collisions between the modules.

4.3. CAD simulations

To validate the theoretical results obtained in the preceding sections, we performed a series of CAD simulations in the KOMPAS 3D software using the computer model from Fig. 1. For this purpose, we selected several points in the workspaces presented in Figs. 7–14. Each point corresponds to a specific relative configuration of the modules, and we checked if the robot could reach the considered configuration. Note that in the CAD software, it is challenging to accurately place the moving platforms relative to each other, especially when they are tilted. To overcome this issue, we first solved the inverse kinematic problem for each selected point and then positioned the carriages of the modules according to the obtained solution. This approach ensures that the relative configuration of the moving platforms meets the selected point.

This section illustrates the results for eight points $G_1, \ldots, G_8$, and Table I presents the values of position parameters x, y, and z and rotation parameters ψ, θ, and σ corresponding to these points. The considered points are selected in the following way:

https://doi.org/10.1017/S0263574725102592 Published online by Cambridge University Press

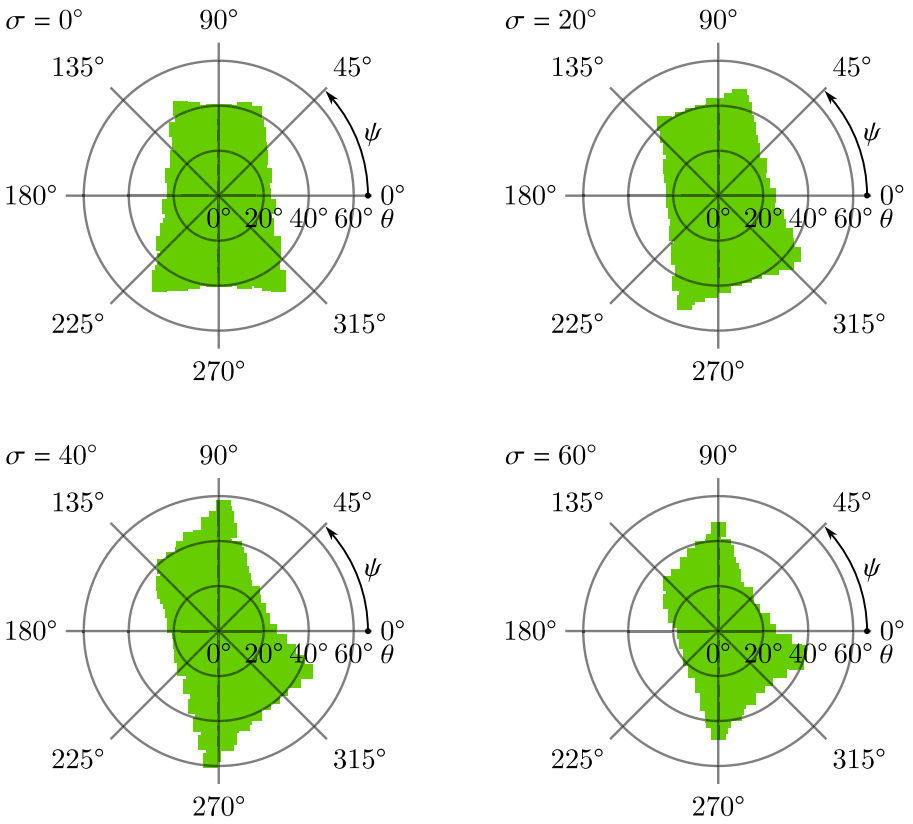


Fig. 11. *Orientation workspace for $x = y = 0$ mm, $z = 150$ mm.*

- Points G_1 and G_2 belong to the top boundary surface of the translation workspace in Fig. 7.
- Points G_3 and G_4 belong to the front boundary edge of the translation workspace in Fig. 10.
- Points G_5 and G_6 belong to the boundaries of the orientation workspace in Fig. 12.
- Points G_7 and G_8 belong to the boundaries of the orientation workspace in Fig. 14.

Table II shows the solution to the inverse kinematic problem for each considered point. We used these data to position the carriages in the developed computer model of the robot. For each point, the obtained relative configuration of the modules met the expected one specified in Table I. Figures 15–22 show the 3D view, front view, and side view of the robot in these configurations, where the right lateral branch of the upper module in the side view is hidden for clarity. The red notations in the figures match the preceding sections and indicate the constraints that limit the workspace in the considered configuration.

As we observe from the figures, these are constraints in the spherical joints that limit the workspace in most cases, that is, the constraints on angles η_{A_i} and η_{B_i} specified in Eqs. (15) and (18).[2] In Fig. 15, the carriages of the two central branches of the upper module reach their highest positions, satisfying Eq. (10); a similar situation is observed in Figs. 16 and 17 for the lateral branches. These results correspond to our selection of points G_1, G_2, and G_3 on the top surface of the workspace (Figs. 7 and 10). Figures 18, 21, and 22 show that the moving platforms of the modules are about to collide with each other. This situation agrees with the selection of points G_4, G_7, and G_8 on the boundaries of the green and red areas in Figs. 10 and 14. It is interesting that the link interference is the only constraint limiting

[2]Angles $\eta_{A\min}$, $\eta_{A\max}$, $\eta_{B\min}$, and $\eta_{B\max}$ in the front and side views of the robot in Figs. 15–22 are shown in a simplified manner because these angles should be measured according to Fig. 3. For example, angle $\eta_{A\max}$ in Fig. 15 is measured in the parallelogram plane.

https://doi.org/10.1017/S0263574725102592 Published online by Cambridge University Press

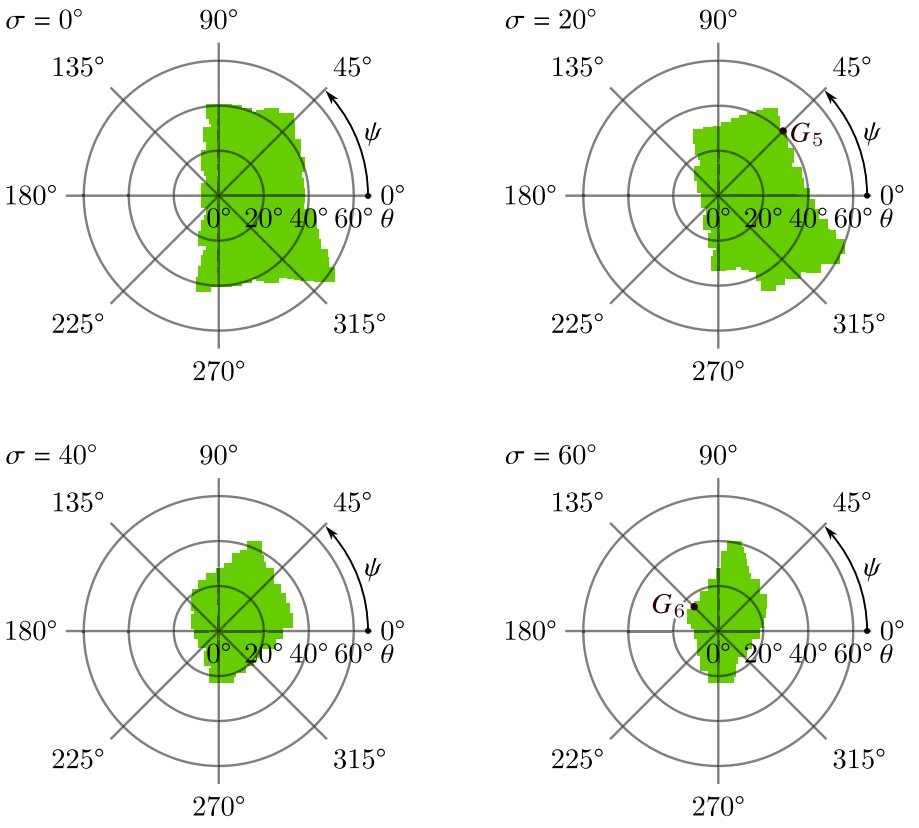


Fig. 12. *Orientation workspace for $x = 100$ mm, $y = 0$ mm, $z = 150$ mm.*

the workspace in Fig. 21: other joint constraints are not violated in this configuration. This result indicates that the link interference of the modules should not be ignored for the correct evaluation of the workspace.

5. Discussion

The methods presented in Sections 3 and 4 allow us to obtain workspaces in the relative motion of two modules. This is a crucial difference from most other papers mentioned in the introduction, where workspaces were considered with respect to the base. On the other hand, analyzing the workspace in the relative motion is more important in practice, for example, in machining, where one module usually displaces the processed part and another module moves the tool. Unlike other methods, the developed techniques allow solving this problem directly without the stage where we need to combine the two workspaces and find their intersection, thereby reducing the computational efforts. Thus, we believe that the proposed methods and obtained results are original and will be valuable for practical applications.

During the workspace analysis, we considered all mechanical constraints existing in the hybrid robot, including the joint constraints and the link interference between the upper and lower modules. Section 4 shows that the link interference significantly affects the workspace and must be included in the workspace analysis. For example, if we ignored the link interference in Fig. 14, we would get the higher tilt angles of the upper moving platform relative to the lower one. These results, however, would be incorrect and could lead to collisions and potential damage of the robot links in real applications.

To analyze these collisions, we applied the GJK algorithm and represented the robot links as convex polytopes. There exist modifications of this algorithm that can deal with general convex objects and rely

https://doi.org/10.1017/S0263574725102592 Published online by Cambridge University Press

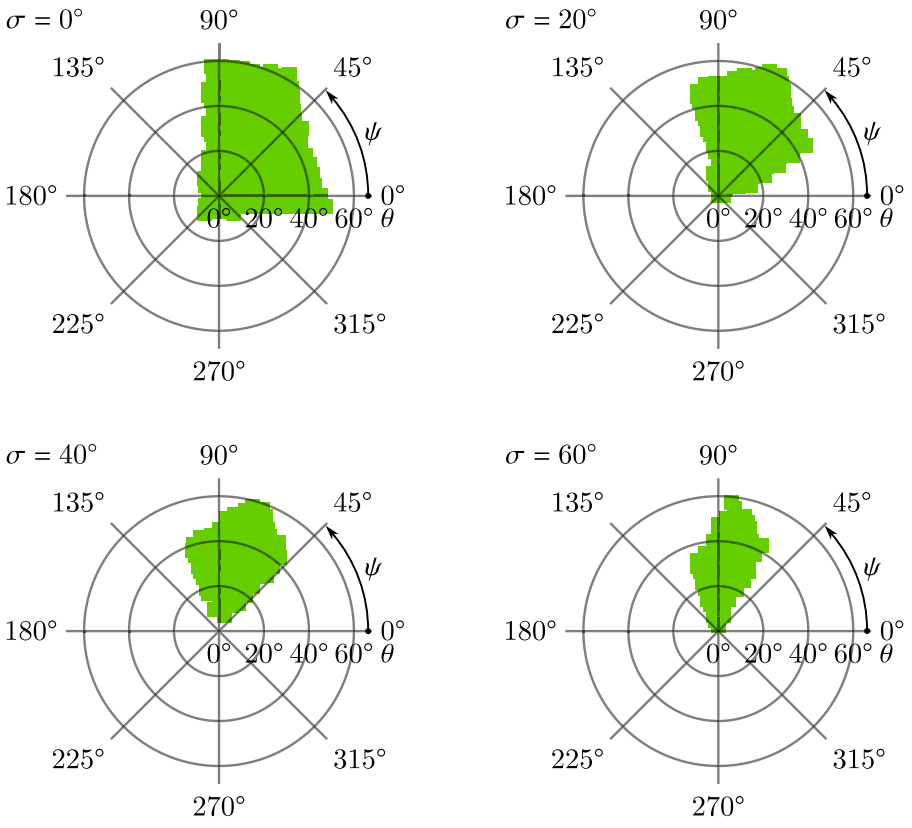


Fig. 13. *Orientation workspace for $x = 100$ mm, $y = 100$ mm, $z = 150$ mm.*

on optimization techniques [61–64]. These methods avoid errors caused by polytope approximations, and they can be used to get more accurate results with less computational efforts. Implementing these techniques in workspace analysis looks promising as well.

The order in which we evaluate mechanical constraints also affects computational efforts. In this paper, we first analyzed the joint constraints and then considered the link interference. We applied this order for illustrative purposes to show the parts of the workspace that meet the joint constraints but violate the link interference (Figs. 7–14). Evaluating the joint constraints requires solving the inverse kinematic problem, as discussed in Sections 3.1–3.3. On the other hand, Sections 3.4.1–3.4.3 show that we do not need to solve this problem to analyze the collisions between the upper platform, the lower platform, and the couplers. These collisions depend only on the relative configuration of the platforms (i.e., on transformation matrix **T**), which is the predefined parameter for the applied discretization approach of the workspace analysis. Thus, by changing the order of constraint evaluation, we can avoid unnecessary computations. In addition, we can ignore the link interference constraint when the upper moving platform is beyond the lower module.

Finally, we should note that singular configurations can divide the workspace into several disjoint regions [65]. For example, in paper [37], we performed the standalone singularity analysis of the 4-DOF upper module and showed that it could not bypass the singularity surface with constant tilt angle φ. The lower module can be used to overcome this problem by adjusting the relative orientation of the moving platforms. At the same time, as we have seen in Section 3.2, there exists at least one singular configuration where the robot loses one rotational DOF in the relative motion, while each module does not meet a singularity. This situation is not typical for conventional parallel or serial robots, which include only a single module [66]. The complete enumeration of these and other singular configurations,

https://doi.org/10.1017/S0263574725102592 Published online by Cambridge University Press

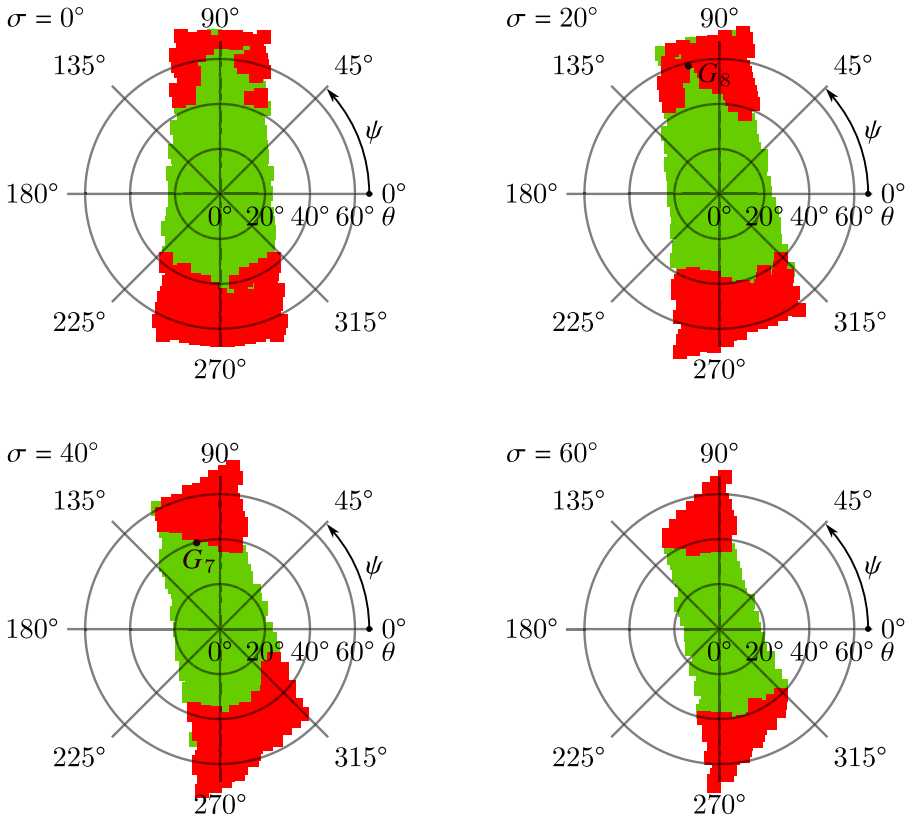


Fig. 14. *Orientation workspace for $x = y = 0$ mm, $z = 75$ mm.*

Table I. *Selected points for CAD simulations.*

Point	x **/ mm**	y **/ mm**	z **/ mm**	ψ **/ deg**	θ **/ deg**	σ **/ deg**
G_1	0	−140	290	0	0	0
G_2	0	140	360	0	0	0
G_3	−130	150	330	30	−30	45
G_4	−100	100	70	30	−30	45
G_5	100	0	150	45	41	20
G_6	100	0	150	135	15	60
G_7	0	0	75	106	40	40
G_8	0	0	75	104	58	20

Table II. *Solution to the inverse kinematics for the selected points.*

Point	h_1 **/ mm**	h_2 **/ mm**	h_3 **/ mm**	h_4 **/ mm**	θ_1 **/ deg**	θ_2 **/ deg**
G_1	853	923	923	853	0	180
G_2	923	832	832	923	0	180
G_3	923	837	782	873	−49	144
G_4	685	608	551	609	−49	144
G_5	698	739	788	711	−35	166
G_6	701	776	742	673	−74	139
G_7	601	663	642	622	−60	169
G_8	585	648	627	577	−42	−164

https://doi.org/10.1017/S0263574725102592 Published online by Cambridge University Press

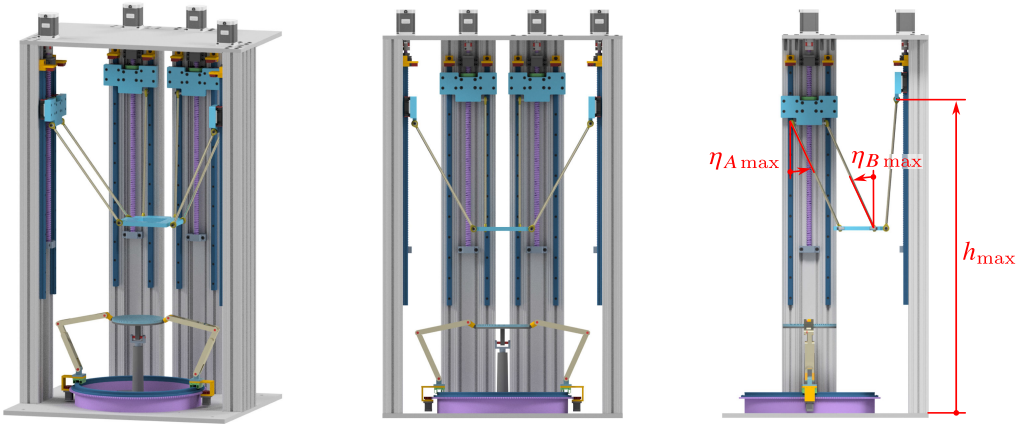


Fig. 15. *Robot configuration corresponding to point G_1.*

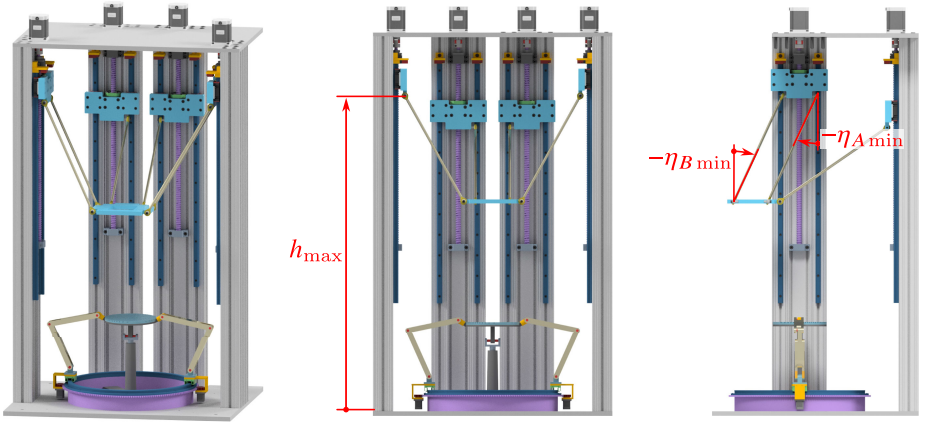


Fig. 16. *Robot configuration corresponding to point G_2.*

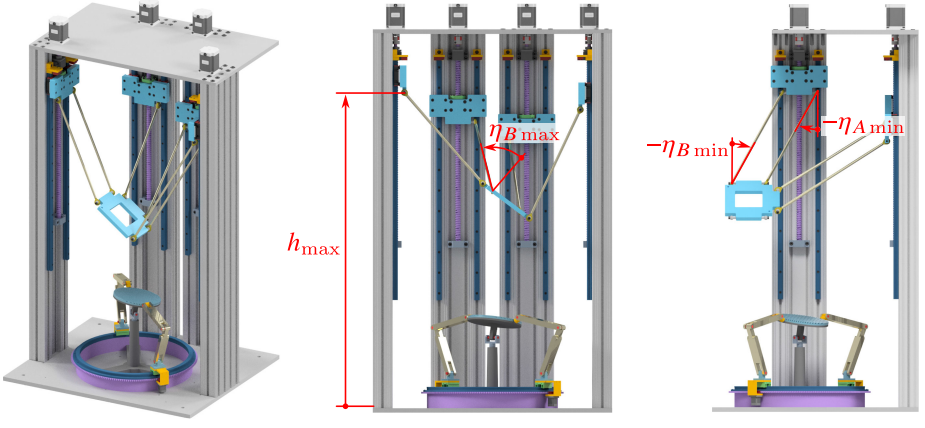


Fig. 17. *Robot configuration corresponding to point G_3.*

https://doi.org/10.1017/S0263574725102592 Published online by Cambridge University Press

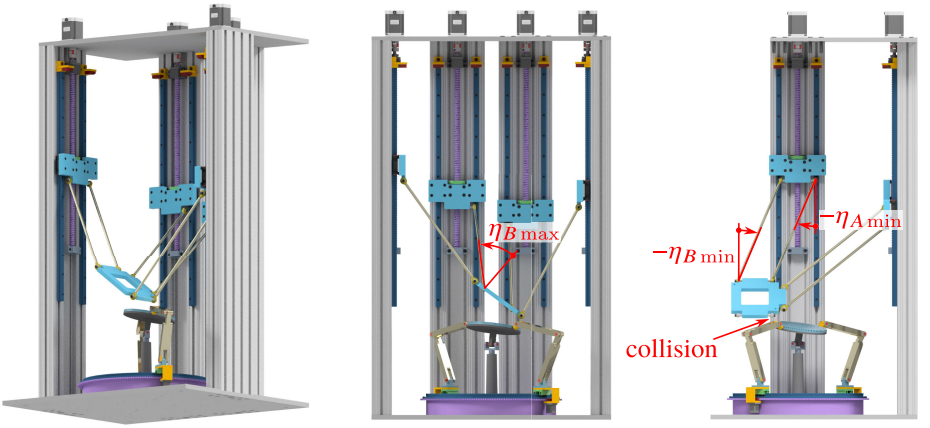


Fig. 18. *Robot configuration corresponding to point G_4.*

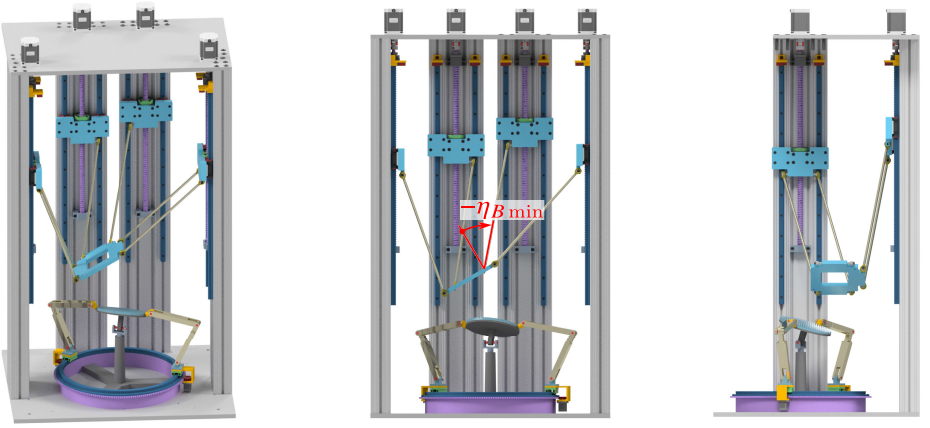


Fig. 19. *Robot configuration corresponding to point G_5.*

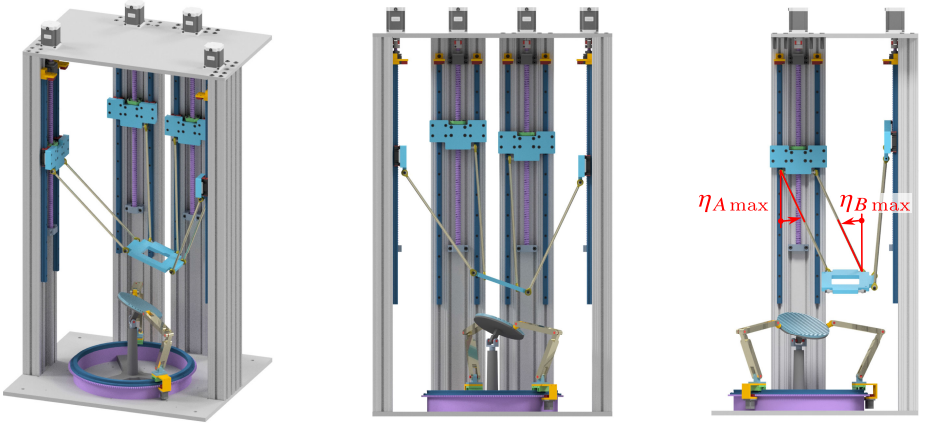


Fig. 20. *Robot configuration corresponding to point G_6.*

https://doi.org/10.1017/S0263574725102592 Published online by Cambridge University Press

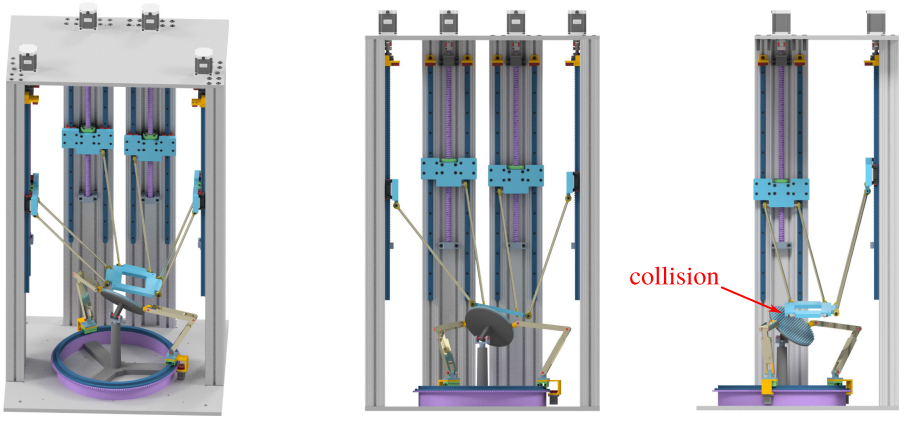


Fig. 21. *Robot configuration corresponding to point G_7.*

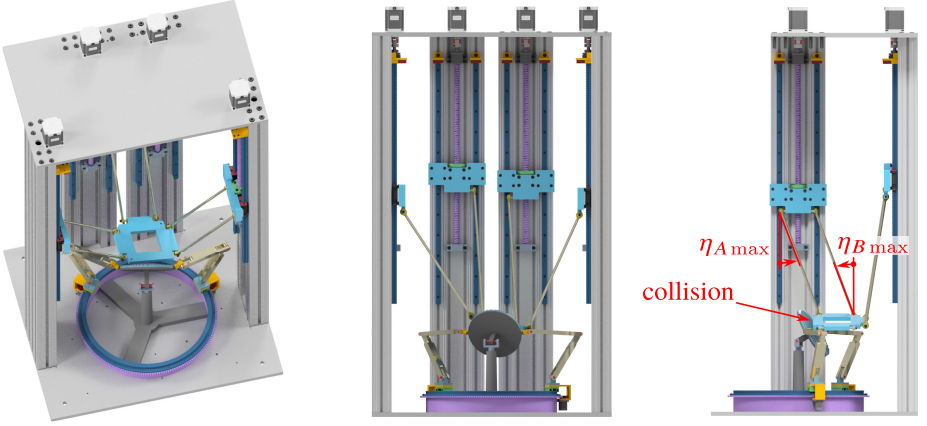


Fig. 22. *Robot configuration corresponding to point G_8.*

as well as estimating the closeness to them [67, 68], requires deriving and analyzing Jacobian matrices, which is beyond this paper and will be the subject of our upcoming studies.

6. Conclusion

The paper performed the workspace analysis of the recently proposed hybrid robot with two parallel modules. One module is a 4-DOF Delta-type parallel mechanism with three translational and one rotational DOFs, and the other module is a 2-DOF rotational parallel mechanism with a circular rail. Thus, the robot has six DOFs in the relative motion of its modules.

In this article, we developed the discretization-based approach that allowed computing the workspace in the relative motion of the modules. The approach relies on the inverse kinematics, for which we provided the closed-form solution, and considers constraints in all joints of the robot, as well as the link interference between the modules. To check the collisions between the links, we represented them as convex polytopes and applied the GJK algorithm.

The proposed techniques were implemented to analyze the translation and orientation workspaces of the hybrid robot. We presented four numerical examples for each workspace and various relative configurations of the modules and analyzed eight specific configurations of the robot in CAD software to validate the developed algorithms. The results indicate that the link interference affects the workspace shape and dimensions and cannot be ignored for correct workspace analysis.

https://doi.org/10.1017/S0263574725102592 Published online by Cambridge University Press

The developed methods are not limited to translation and orientation workspaces but can be used to compute other types of workspaces as well. These methods are also applicable to other hybrid robots composed of two modules. In future studies, we will include singular configurations to the workspace analysis and use the obtained results for trajectory planning and optimal design of the robot.

Author contributions. AA and AF conceived and designed the study. KM and AA devised the workspace analysis method and performed simulations in Julia. KM, AF, and AA prepared graphical material and wrote the manuscript. AA and AF supervised the article.

Data availability statement. Julia program that performs the workspace analysis according to the proposed algorithms is available free online at https://doi.org/10.17632/vsvvd83gpy.1.

Funding statement. This research was supported by the Russian Science Foundation under grant no. 22-79-10304, https://rscf.ru/en/project/22-79-10304/.

Competing interests. The authors declare that no conflicts of interest exist.

Ethical approval. Not applicable.

References

[1] B. Wang, P. Li, C. Yang, X. Hu and Y. Zhao, "Robotica: decoupled elastostatic stiffness modeling of hybrid robots," *Robotica* **42**(7), 2309–2327 (2024). doi: 10.1017/S0263574724000675.
[2] S. Kumar, A. Müller and F. Kirchner, *Biologically Inspired Series-Parallel Hybrid Robots* (Academic Press, London, 2025). doi: 10.1016/C2020-0-02362-5.
[3] N. Van Toan and P. B. Khoi, "A control solution for closed-form mechanisms of relative manipulation based on fuzzy approach," *Int. J. Adv. Robot. Syst.* **16**(2) (2019). doi: 10.1177/1729881419839810.
[4] V. A. Glazunov, A. B. Lastochkin, K. A. Shalyukhin and P. O. Danilin, "Analysis and classification of relative manipulation devices," *J. Mach. Manuf. Reliab.* **38**(4), 379–382 (2009). doi: 10.3103/S1052618809040141.
[5] Y. Wu, H. Wang and Z. Li, "Quotient kinematics machines: concept, analysis, and synthesis," *J. Mech. Robot.* **3**(4), 041004 (2011). doi: 10.1115/1.4004891.
[6] H. Huang, Z. Deng, B. Li and R. Liu, "Analysis and synthesis of a kind of mobility reconfigurable robot with multi-task capability," *J. Adv. Mech. Des. Syst. Manuf.* **5**(2), 87–102 (2011). doi: 10.1299/jamdsm.5.87.
[7] L. Carbonari, M. Callegari, G. Palmieri and M.-C. Palpacelli, "A new class of reconfigurable parallel kinematic machines," *Mech. Mach. Theory* **79**, 173–183 (2014). doi: 10.1016/j.mechmachtheory.2014.04.011.
[8] Q. Liu, H. Liu, J. Xiao, W. Tian, Y. Ma and B. Li, "Open-architecture of CNC system and mirror milling technology for a 5-axis hybrid robot," *Robot. Comput. Integr. Manuf.* **81**, 102504 (2023). doi: 10.1016/j.rcim.2022.102504.
[9] S. Ma, J. Xiao, H. Liu, S. Liu and Y. Tian, "Modeling and analysis for time-varying dynamics of thin-walled workpieces in mirror milling considering material removal," *Sci. China Technol. Sci.* **66**(7), 1883–1898 (2023). doi: 10.1007/s11431-022-2360-6.
[10] M. Dogar, A. Spielberg, S. Baker and D. Rus, "Multi-robot grasp planning for sequential assembly operations," *Auton. Robots* **43**(3), 649–664 (2019). doi: 10.1007/s10514-018-9748-z.
[11] Y. He, M. Wu and S. Liu, "A cooperative optimization strategy for distributed multi-robot manipulation with obstacle avoidance and internal performance maximization," *Mechatronics* **76**, 102560 (2021). doi: 10.1016/j.mechatronics.2021.102560.
[12] M. A. Isa and I. Lazoglu, "Five-axis additive manufacturing of freeform models through buildup of transition layers," *J. Manuf. Syst.* **50**, 69–80 (2019). doi: 10.1016/j.jmsy.2018.12.002.
[13] D. Zhao, G. Zhu, J. He and W. Guo, "An initial feasibility study into ray-based slicing for revolving thin-wall parts using a rotary 3D printer," *Rapid Prototyp. J.* **29**(1), 128–144 (2023). doi: 10.1108/RPJ-09-2021-0226.
[14] H. Saeidi, J. D. Opfermann, M. Kam, S. Wei, S. Leonard, M. H. Hsieh, J. U. Kang and A. Krieger, "Autonomous robotic laparoscopic surgery for intestinal anastomosis," *Sci. Robot.* **7**(62), eabj2908 (2022). doi: 10.1126/scirobotics.abj2908.
[15] A. Asadizeidabadi, S. Hosseini, F. Vetshev, S. Osminin and S. Hosseini, "Comparison of da Vinci 5 with previous versions of da Vinci and Sina: a review," *Laparosc. Endosc. Robot. Surg.* **7**(2), 60–65 (2024). doi: 10.1016/j.lers.2024.04.006.
[16] M. Russo and M. Ceccarelli, "A geometrical formulation for the workspace of parallel manipulators," *Robotica* **40**(8), 2581–2591 (2022). doi: 10.1017/S0263574721001806.
[17] F. Ennaiem, A. Chaker, J. Sandoval, A. Mlika, L. Romdhane, S. Bennour, S. Zeghloul and M. A. Laribi, "A hybrid cable-driven parallel robot as a solution to the limited rotational workspace issue," *Robotica* **41**(3), 850–868 (2023). doi: 10.1017/S0263574722000923.
[18] Q. Li, C. Yang, L. Xu and W. Ye, *Performance Analysis and Optimization of Parallel Manipulators* (Springer, Singapore, 2023). doi: 10.1007/978-981-99-0542-3.

https://doi.org/10.1017/S0263574725102592 Published online by Cambridge University Press

[19] K. Erastova, "Effective workspaces of parallel robots," *Robotica* **40**(12), 4308–4325 (2022). doi: 10.1017/S0263574722000911.

[20] A. Rosyid, B. El-Khasawneh and A. Alazzam, "Review article: performance measures of parallel kinematics manipulators," *Mech. Sci.* **11**(1), 49–73 (2020). doi: 10.5194/ms-11-49-2020.

[21] L.-W. Tsai and S. Joshi, "Kinematic analysis of 3-DOF position mechanisms for use in hybrid kinematic machines," *J. Mech. Des.* **124**(2), 245–253 (2002). doi: 10.1115/1.1468860.

[22] S. Kucuk, "Dexterous workspace optimization for a new hybrid parallel robot manipulator," *J. Mech. Robot.* **10**(6), 064503 (2018). doi: 10.1115/1.4041334.

[23] A. N. Chaudhury and A. Ghosal, "Optimum design of multi-degree-of-freedom closed-loop mechanisms and parallel manipulators for a prescribed workspace using Monte Carlo method," *Mech. Mach. Theory* **118**, 115–138 (2017). doi: 10.1016/j.mechmachtheory.2017.07.021.

[24] D. Zhang and B. Wei, "Modelling and optimisation of a 4-DOF hybrid robotic manipulator," *Int. J. Comput. Integr. Manuf.* **30**(11), 1179–1189 (2017). doi: 10.1080/0951192X.2017.1305505.

[25] H. Ye, D. Wang, J. Wu, Y. Yue and Y. Zhou, "Forward and inverse kinematics of a 5-DOF hybrid robot for composite material machining," *Robot. Comput. Integr. Manuf.* **65**, 101961 (2020). doi: 10.1016/j.rcim.2020.101961.

[26] J. Smits, D. Reynaerts and E. V. Poorten, "Synthesis and methodology for optimal design of a parallel remote center of motion mechanism: application to robotic eye surgery," *Mech. Mach. Theory* **151**, 103896 (2020). doi: 10.1016/j.mechmachtheory.2020.103896.

[27] D. Pisla, A. Szilaghyi, C. Vaida and N. Plitea, "Kinematics and workspace modeling of a new hybrid robot used in minimally invasive surgery," *Robot. Comput. Integr. Manuf.* **29**(2), 463–474 (2013). doi: 10.1016/j.rcim.2012.09.016.

[28] A. Rastegarpanah, H. Rakhodaei, M. Saadat, M. Rastegarpanah, N. Marturi, A. Borboni and R. C. V. Loureiro, "Path-planning of a hybrid parallel robot using stiffness and workspace for foot rehabilitation," *Adv. Mech. Eng.* **10**(1) (2018). doi: 10.1177/1687814017754159.

[29] L.-T. Schreiber and C. Gosselin, "Kinematically redundant planar parallel mechanisms: kinematics, workspace and trajectory planning," *Mech. Mach. Theory* **119**, 91–105 (2018). doi: 10.1016/j.mechmachtheory.2017.08.022.

[30] P. Xu, C. F. Cheung, C. Wang and C. Zhao, "Novel hybrid robot and its processes for precision polishing of freeform surfaces," *Precis. Eng.* **64**, 53–62 (2020). doi: 10.1016/j.precisioneng.2020.03.013.

[31] H. Zhang, H. Fang, Y. Fang and B. Jiang, "Workspace analysis of a hybrid kinematic machine tool with high rotational applications," *Math. Probl. Eng.* **2018**, 2607497 (2018). doi: 10.1155/2018/2607497.

[32] Z. Qin, Z. Liu, Y. Liu, H. Gao, C. Sun and G. Sun, "Workspace analysis and optimal design of dual cable-suspended robots for construction," *Mech. Mach. Theory* **171**, 104763 (2022). doi: 10.1016/j.mechmachtheory.2022.104763.

[33] I. Chawla, P. M. Pathak, L. Notash, A. K. Samantaray, Q. Li and U. K. Sharma, "Workspace analysis and design of large-scale cable-driven printing robot considering cable mass and mobile platform orientation," *Mech. Mach. Theory* **165**, 104426 (2021). doi: 10.1016/j.mechmachtheory.2021.104426.

[34] K. Mukhin, A. Antonov and A. Fomin, "Mechanism design and inverse kinematics of a 6-DOF hybrid robot with two parallel modules," **In:** *Robotics and Mechatronics* (L. Romdhane, A. Mlika, S. Zeghloul, A. Chaker and M. A. Laribi, eds.) (Springer, Cham, 2024) pp. 309–318. doi: 10.1007/978-3-031-59888-3_28.

[35] P. A. Laryushkin, K. G. Erastova, G. S. Filippov and S. V. Kheylo, "Calculation of Delta-type mechanisms with linear actuators and different numbers of degrees of freedom," *J. Mach. Manuf. Reliab.* **48**(3), 204–210 (2019). doi: 10.3103/S1052618819030105.

[36] P. A. Laryushkin, "Experimental study of force transfer in a Delta-type mechanism with four degrees of freedom," *J. Mach. Manuf. Reliab.* **50**(5), 379–387 (2021). doi: 10.3103/S1052618821050071.

[37] P. Laryushkin, A. Fomin and A. Antonov, "Kinematic and singularity analysis of a 4-DOF Delta-type parallel robot," *J. Braz. Soc. Mech. Sci. Eng.* **45**(4), 218 (2023). doi: 10.1007/s40430-023-04128-7.

[38] P. Laryushkin, A. Fomin, A. Antonov and V. Glazunov, "Virtual and physical prototyping of the 4-DOF Delta-type parallel robot based on the criteria of closeness to singularity," **In:** *Proceedings of MSR-RoManSy 2024* (P. Larochelle, J. M. McCarthy and C. P. Lusk, eds.) (Springer, Cham, 2024) pp. 167–178. doi: 10.1007/978-3-031-60618-2_14.

[39] C. C. Xu, C. Xue and X. C. Duan, "A novel 2R parallel mechanism for alt-azimuth pedestal," *IOP Conf. Ser. Mater. Sci. Eng.* **428**(1), 012053 (2018). doi: 10.1088/1757-899X/428/1/012053.

[40] S. He, X. Duan, X. Qu and J. Xiao, "Kinematic modeling and motion control of a parallel robotic antenna pedestal," *Robotica* **41**(11), 3275–3295 (2023). doi: 10.1017/S0263574723000917.

[41] P. Laryushkin, A. Antonov, A. Fomin and V. Glazunov, "Novel reconfigurable spherical parallel mechanisms with a circular rail," *Robotics* **11**(2), 30 (2022). doi: 10.3390/robotics11020030.

[42] P. Laryushkin, A. Antonov, A. Fomin and V. Glazunov, "Inverse and forward kinematics of a reconfigurable spherical parallel mechanism with a circular rail," **In:** *ROMANSY 24 - Robot Design, Dynamics and Control* (A. Kecskeméthy and V. Parenti-Castelli, eds.) (Springer, Cham, 2022) pp. 246–254. doi:10.1007/978-3-031-06409-8_26.

[43] I. V. Brem, P. A. Laryushkin, A. S. Fomin and A. V. Antonov, "Design, mobility and kinematic analysis of a 4-DOF 3R1T redundantly actuated foldable parallel manipulator with a circular rail," **In:** *Proceedings of the 2024 6th International Conference on Reconfigurable Mechanisms and Robots (ReMAR)* (Chicago, IL, USA, 2024) pp. 309–314. doi: 10.1109/ReMAR61031.2024.10617927.

[44] Y. Shen, J. Ren, N. Huang, Y. Zhang, X. Zhang and L. Zhu, "Surface form inspection with contact coordinate measurement: A review," *Int. J. Extrem. Manuf.* **5**(2), 022006 (2023). doi: 10.1088/2631-7990/acc76e.

[45] H. Shang, C. Liu and R. Wang, "Measurement methods of 3D shape of large-scale complex surfaces based on computer vision: a review," *Measurement* **197**, 111302 (2022). doi: 10.1016/j.measurement.2022.111302.

https://doi.org/10.1017/S0263574725102592 Published online by Cambridge University Press

[46] S. N. Nabavi, A. Akbarzadeh and J. Enferadi, "A study on kinematics and workspace determination of a general 6-PUS robot," *J. Intell. Robot. Syst.* **91**(3–4), 351–362 (2018). doi: 10.1007/s10846-017-0704-5.
[47] Y. Zhou, J. Niu, Z. Liu and F. Zhang, "A novel numerical approach for workspace determination of parallel mechanisms," *J. Mech. Sci. Technol.* **31**(6), 3005–3015 (2017). doi: 10.1007/s12206-017-0544-z.
[48] S. Modak and R. K. K, "Kinematics and singularity analysis of a novel hybrid industrial manipulator," *Robotica* **42**(2), 579–610 (2024). doi: 10.1017/S0263574723001662.
[49] Y. Cao, Z. Huang, H. Zhou and W. Ji, "Orientation workspace analysis of a special class of the Stewart–Gough parallel manipulators," *Robotica* **28**(7), 989–1000 (2010). doi: 10.1017/S0263574709990841.
[50] I. A. Bonev and C. M. Gosselin, "Analytical determination of the workspace of symmetrical spherical parallel mechanisms," *IEEE Trans. Robot.* **22**(5), 1011–1017 (2006). doi: 10.1109/TRO.2006.878983.
[51] K. M. Lynch and F. C. Park, *Modern Robotics: Mechanics, Planning, and Control* (Cambridge University Press, Cambridge, 2017). doi: 10.1017/9781316661239.
[52] P. Jiménez, F. Thomas and C. Torras, "3D collision detection: a survey," *Comput. Graph.* **25**(2), 269–285 (2001). doi: 10.1016/S0097-8493(00)00130-8.
[53] S. Kockara, T. Halic, K. Iqbal, C. Bayrak and R. Rowe, "Collision detection: a survey," **In:** *Proceedings of the 2007 IEEE International Conference on Systems, Man and Cybernetics* (Montreal, QC, Canada, 2007) pp. 4046–4051. doi: 10.1109/ICSMC.2007.4414258.
[54] E. G. Gilbert, D. W. Johnson and S. S. Keerthi, "A fast procedure for computing the distance between complex objects in three-dimensional space," *IEEE J. Robot. Autom.* **4**(2), 193–203 (1988). doi: 10.1109/56.2083.
[55] G. Van den Bergen, "A fast and robust GJK implementation for collision detection of convex objects," *J. Graph. Tools* **4**(2), 7–25 (1999). doi: 10.1080/10867651.1999.10487502.
[56] C. Ericson, *Real-Time Collision Detection* (CRC Press, Boca Raton, 2004). doi: 10.1201/b14581.
[57] L. Montaut, Q. L. Lidec, V. Petrik, J. Sivic and J. Carpentier, "Collision detection accelerated: an optimization perspective," **In:** *Robotics: Science and Systems* (New York City, NY, USA, 2022). doi: 10.15607/RSS.2022.XVIII.039.
[58] J.-P. Merlet, *Parallel Robots*, 2nd ed. (Springer, Dordrecht, 2006). doi: 10.1007/1-4020-4133-0.
[59] I. A. Bonev, D. Zlatanov and C. M. Gosselin, "Advantages of the modified Euler angles in the design and control of PKMs," **In:** *Proceedings of the 2002 Parallel Kinematic Machines International Conference* (Chemnitz, 2002) pp. 171–188. https://scholar.google.com/scholar?cluster=6499751952328294897.
[60] J. Bezanson, A. Edelman, S. Karpinski and V. B. Shah, "Julia: a fresh approach to numerical computing," *SIAM Rev.* **59**(1), 65–98 (2017). doi: 10.1137/141000671.
[61] E. G. Gilbert and C.-P. Foo, "Computing the distance between general convex objects in three-dimensional space," *IEEE Trans. Robot. Autom.* **6**(1), 53–61 (1990). doi: 10.1109/70.88117.
[62] S. Cameron, "Enhancing GJK: computing minimum and penetration distances between convex polyhedra," **In:** *Proceedings of the 1997 IEEE International Conference on Robotics and Automation* **4** (Albuquerque, NM, USA, 1997) pp. 3112–3117. doi:10.1109/ROBOT.1997.606761.
[63] M. Montanari, N. Petrinic and E. Barbieri, "Improving the GJK algorithm for faster and more reliable distance queries between convex objects," *ACM Trans. Graph* **36**(3), 1–17 (2017). doi: 10.1145/3083724.
[64] L. Montaut, Q. L. Lidec, V. Petrik, J. Sivic and J. Carpentier, "GJK++: leveraging acceleration methods for faster collision detection," *IEEE Trans. Robot.* **40**, 2564–2581 (2024). doi: 10.1109/TRO.2024.3386370.
[65] A. M. Kolte, S. Ramesh and S. Bandyopadhyay, "Analytical derivation of singularity-free tubes in the constant-orientation workspace of 6-6 Stewart platform manipulators," *Robotica* **42**(11), 3839–3866 (2024). doi: 10.1017/S026357472400167X.
[66] M. Conconi and M. Carricato, "A new assessment of singularities of parallel kinematic chains," *IEEE Trans. Robot.* **25**(4), 757–770 (2009). doi: 10.1109/TRO.2009.2020353.
[67] P. A. Voglewede and I. Ebert-Uphoff, "Overarching framework for measuring closeness to singularities of parallel manipulators," *IEEE Trans. Robot.* **21**(6), 1037–1045 (2005). doi: 10.1109/TRO.2005.855993.
[68] W. Bu, "Closeness to singularities of manipulators based on geometric average normalized volume spanned by weighted screws," *Robotica* **35**(7), 1616–1626 (2017). doi: 10.1017/S0263574716000345.

Cite this article: K. Mukhin, A. Antonov and A. Fomin (2025). "Workspace analysis of a 6-degree-of-freedom hybrid robot with two parallel modules", Robotica **43**, 3976–4004. https://doi.org/10.1017/S0263574725102592

https://doi.org/10.1017/S0263574725102592 Published online by Cambridge University Press